

NASA/TP-2018-219838



From S-N to the Paris Law with a New Mixed-Mode Cohesive Fatigue Model

Carlos G. Dávila
Langley Research Center, Hampton, Virginia

June 2018

NASA STI Program . . . in Profile

Since its founding, NASA has been dedicated to the advancement of aeronautics and space science. The NASA scientific and technical information (STI) program plays a key part in helping NASA maintain this important role.

The NASA STI program operates under the auspices of the Agency Chief Information Officer. It collects, organizes, provides for archiving, and disseminates NASA's STI. The NASA STI program provides access to the NTRS Registered and its public interface, the NASA Technical Reports Server, thus providing one of the largest collections of aeronautical and space science STI in the world. Results are published in both non-NASA channels and by NASA in the NASA STI Report Series, which includes the following report types:

- **TECHNICAL PUBLICATION.** Reports of completed research or a major significant phase of research that present the results of NASA Programs and include extensive data or theoretical analysis. Includes compilations of significant scientific and technical data and information deemed to be of continuing reference value. NASA counter-part of peer-reviewed formal professional papers but has less stringent limitations on manuscript length and extent of graphic presentations.
- **TECHNICAL MEMORANDUM.** Scientific and technical findings that are preliminary or of specialized interest, e.g., quick release reports, working papers, and bibliographies that contain minimal annotation. Does not contain extensive analysis.
- **CONTRACTOR REPORT.** Scientific and technical findings by NASA-sponsored contractors and grantees.

- **CONFERENCE PUBLICATION.** Collected papers from scientific and technical conferences, symposia, seminars, or other meetings sponsored or co-sponsored by NASA.
- **SPECIAL PUBLICATION.** Scientific, technical, or historical information from NASA programs, projects, and missions, often concerned with subjects having substantial public interest.
- **TECHNICAL TRANSLATION.** English-language translations of foreign scientific and technical material pertinent to NASA's mission.

Specialized services also include organizing and publishing research results, distributing specialized research announcements and feeds, providing information desk and personal search support, and enabling data exchange services.

For more information about the NASA STI program, see the following:

- Access the NASA STI program home page at <http://www.sti.nasa.gov>
- E-mail your question to help@sti.nasa.gov
- Phone the NASA STI Information Desk at 757-864-9658
- Write to:
NASA STI Information Desk
Mail Stop 148
NASA Langley Research Center
Hampton, VA 23681-2199

NASA/TP-2018-219838



From S-N to the Paris Law with a New Mixed-Mode Cohesive Fatigue Model

Carlos G. Dávila
Langley Research Center, Hampton, Virginia

National Aeronautics and
Space Administration

Langley Research Center
Hampton, Virginia 23681-2199

June 2018

The use of trademarks or names of manufacturers in the report is for accurate reporting and does not constitute an official endorsement, either expressed or implied, of such products or manufacturers by the National Aeronautics and Space Administration.

Available from:

NASA STI Program / Mail Stop 148
NASA Langley Research Center
Hampton, VA 23681-2199
Fax: 757-864-6500

Contents

Abstract	1
1 Introduction	1
2 A Cohesive Fatigue Model Based on an Assumed S-N Diagram	4
2.1 S-N Diagram for Matrix Tension	5
2.2 Estimating the Endurance Limit	5
2.3 Effect of Stress Ratio R on Endurance Limit	6
2.4 Cohesive Fatigue Damage Model	8
2.5 Determination of Coefficients β and γ for IM7/8552	10
2.6 Residual Strength	12
2.7 Mixed Mode	12
2.8 Predicting Crack Propagation with Simplified Cyclic Loading (SCL)	15
3 Validation: Crack Propagation in Mode I and Mixed Mode	16
3.1 Analysis of Double Cantilever Beam Specimen	16
3.1.1 Finite Element Model of DCB Specimen	16
3.1.2 Predicting Paris Law Propagation Rate	18
3.1.3 Bridging and R-curve Effects	20
3.1.4 Predicting the Effect of the R Ratio on the Paris Law	24
3.1.5 Analysis of Propagation Onset	25
3.2 Analysis of the Mixed Mode Bending Test	26
3.3 Relationships between Material Properties	28
4 Summary and Discussion	30
References	31
Appendix A: Numerical Determination of Fatigue Damage Coefficients β and γ	34

Abstract

The relationship between fatigue life and fatigue crack propagation rate is explored with a new cohesive damage model. The parameters of the model are obtained from idealizations of S-N diagrams used in engineering design. The model is based on the hypothesis that both stable tearing damage and damage due to cyclic loading are representations of a density of microcracks and, therefore, a single damage variable can describe the state of damage. This assumption implies that the quasi-static cohesive law that describes tearing is also the envelope of the fatigue damage. Fatigue damage within the cohesive envelope is assumed to accumulate at a rate that depends on the displacement jumps. The fatigue model was implemented as a UMAT subroutine for Abaqus cohesive elements by adding fatigue damage accumulation to a cohesive model based on the Turon mixed-mode cohesive laws. The analyses were conducted using a simplified cyclic loading procedure in which the maximum applied load is kept constant and the computational expense of cycling the load is avoided. The predicted propagation rates in mode I and mixed mode were compared to experimental results for IM7/8552 graphite/epoxy tape. Several aspects of the results were investigated, including the effect of R-curves, the stress ratio R , and the difference between displacement control and force control.

1 Introduction

Engineering calculations of fatigue life are usually performed using stress-life diagrams, called S-N curves [1, 2]. These curves represent the number of cycles that a material can sustain at a given stress level before failure. The data to generate these curves is obtained by cycling smooth or notched specimens until failure. The S-N curves of many materials are simple and can be approximated by straight lines in a log-log plot. In addition, analysis techniques have been developed to account for the effect of the ratio of the minimum to the maximum stress on the S-N curves. Since these calculations essentially depend on the knowledge of the stress state, predicting fatigue life with S-N diagrams does not require specialized computational tools.

On the other hand, predicting fatigue crack propagation is significantly more difficult. First, fracture mechanics tools are required because the rate of crack propagation, defined as a crack extension, da , per incremental number of cycles, dN , is a function of the energy release rate (ERR), G . The rate of crack propagation in fatigue is often described with the Paris law:

$$\frac{da}{dN} = C(G)^m \quad (1)$$

where G is the ERR and C and m are material constants that vary with stress ratio and mode mixity. When Eq. 1 is plotted on log-log axes, it appears as a straight line relating da/dN to G . In the remainder of this report, the term “Paris law” will refer to this line rather than to the specific form of Eq. 1.

The virtual crack closure technique (VCCT) within the finite element method (FEM) is the methodology typically used to calculate the ERR from finite element results [3]. When G exceeds a critical value G_c , the ties that hold the crack tip closed are released and the crack is allowed to propagate. Under cyclic loading, the ERR is used to calculate the rate of propagation using with Eq. 1. Recent enhancements to VCCT in commercial finite element software suites automate the simulation of crack propagation by releasing the constraints that initially tie the two crack surfaces together [4]. However, commercial tools still have difficulty propagating cracks in three dimensions when the crack front is not aligned with the finite element mesh. In the case of misalignment of the front, it is necessary to implement a gradual release of the forces that tie the surfaces together at the front. Without a gradual release, the predicted delamination fronts are jagged, and the delaminations propagate at lower loads than delaminations with smooth fronts [5]. Techniques to achieve this gradual release have recently been implemented in Abaqus [4]. In fatigue, gradual release procedures have only recently been demonstrated [6]. Finally, linear elastic fracture mechanics (LEFM) techniques such as the VCCT require an initial crack and the criterion is valid only after the crack length has reached a certain length. LEFM cannot predict crack nucleation, and the load required for the propagation of very short cracks is overestimated [7].

Cohesive element formulations to predict the nucleation and propagation of cracks in composite structures subjected to cyclic fatigue have also been the subject of intense development for almost two decades. The main difficulty in the development of a cohesive fatigue damage model consists in linking the damage variable, d , to the crack propagation rate [8]. Turon's fatigue model [9] proposes linking the two as follows:

$$\frac{dd}{dN} = \frac{1}{l_{pz}} \frac{(\Delta^f (1-d) + \Delta^c d)^2}{\Delta^f \Delta^c} \frac{da}{dN} \quad (2)$$

where dd/dN is the rate of change of the damage variable, l_{pz} is the length of the process zone, i.e., the zone where the damage is partially developed, Δ^f is the maximum displacement jump of the cohesive law, Δ^c is the displacement jump for damage initiation, and da/dN is the propagation rate expressed by the Paris law. The damage variable is defined such that $(1-d)$ is the ratio of the damaged stiffness over the initial stiffness of the cohesive law. The length of the process zone appears in this expression because the damage variable at any particular point along the path of the crack must gradually increase from zero to one as the entire process zone traverses that point. Therefore, for a given da/dN , the longer the l_{pz} , the larger number of cycles for the damage variable to reach one. Since the fatigue damage rate at a material point depends on the damage state at other locations, the model described by Eq. 2 is nonlocal.

In Turon's initial fatigue model, l_{pz} was calculated with an analytical expression and supplied to the constitutive model as a material property. However, l_{pz} is equal to the characteristic length of a material only when the structural dimensions can be considered infinite. In common structural problems, l_{pz} can change, for instance, with the thickness of the adherends and mode mixity. Furthermore, there are no analytical expressions for l_{pz} in fatigue. These difficulties can be eliminated using a contour J -integral, as proposed by Bak [10]. However, this implementation is complex and has only been demonstrated for two-dimensional problems.

Iarve [11] proposed a model that eliminated the problem of the l_{pz} and the nonlocal aspects of an implementation of the Paris law based on cohesive laws by assuming that all of the fatigue damage is concentrated at the elements along the crack front. Therefore, in Iarve's model, the length of the fatigue process zone is set equal to the length of the element. In addition, Iarve included the important effect of the strength reduction due to fatigue. This reduction is necessary for problems with mild stress concentrations, where failure of the material can occur even when the static strength is not exceeded. Iarve uses an S-N diagram to initiate damage, at which point the quasi-static cohesive law is updated as follows: the initiation strength is reduced to the stress at which the initiation of damage was triggered, and the cohesive law is redrawn such that the area under the curve remains unchanged and equal to G_c .

The approach proposed by Voormeeren et al. [12] for predicting fatigue crack propagation eliminates the need for a damage evolution law by using a "thick level set" formulation that updates damage continuously under a crack front that moves with a velocity prescribed by the Paris law. The method is elegant, but it has not yet been demonstrated in three-dimensional problems due to the complexity of the implementation.

As the preceding examples illustrate, the implementation of a general methodology for fatigue crack propagation based on the Paris law with VCCT or with cohesive elements is equally difficult. The former cannot be used to initiate cracks and has difficulties with delamination fronts that are not aligned with the mesh. The latter leads to the problem of the non-locality of the Paris law with respect to the process zone with the unintuitive aspect of damage models that require information from locations away from the point of interest. In addition to these implementation issues, there are a number of unknown issues regarding the Paris law that have not been resolved. For instance, a Paris law that accounts for mode mixity, stress ratio R , and R-curve increases in the energy release rate has not been properly demonstrated, mostly because of the high cost of performing a full experimental characterization. Considering that some specimens require several million cycles, times the number of replicates, mixed-mode ratios, and stress ratios to be considered, leads to hundreds of millions of cycles, requiring years of continuous testing for one material. In addition, questions remain about whether the Paris law is a true material property or if it is instead an approximation to a structural response that may depend on specimen dimensions, loading history, or other phenomena.

On the other hand, a number of local damage models that attempt to predict fatigue crack propagation without the Paris law have also been proposed. In fact, most of the earlier cohesive fatigue models were local formulations. For instance, nearly two decades ago, Peerlings [13] proposed a phenomenological model in which da/dN is a function of the local strain. Similarly, Nguyen demonstrated that a cohesive model that accounts for the near-tip plastic fields in metals can predict the straight lines of the Paris law [14]. Maiti [15] introduced a two-parameter law for mode I damage accumulation in which the coefficients of the law could be related to the slope of the Paris law. Although most of these local damage models ignore the strength reduction issues in fatigue in favor of the rate of propagation, Nojavan [16] proposed a local model for mixed-mode delamination in which an S-N response is used to initiate damage. After initiation, an empirical expression based on the displacement jumps is used to accumulate damage. As in all of the local models presented in the literature, the coefficients of the damage model are determined by trial and

error by comparing the predictions with experimental results. The review by Bak et al. [17] of experimental observations also provides an insightful classification of various fatigue models and their predictive capabilities.

Damage may be interpreted at the microscale as the creation of microsurfaces and discontinuities that cause a reduction of the elastic stiffness and the eventual load-carrying ability of the material [18]Lemaitre, 1996. This damage may be the result of tearing, i.e., a mode of fracture that requires work for propagation, or damage can be the result of cyclic loading. A heuristic fatigue damage model is proposed herein that is based on the hypothesis that damage at a material point is due to either tearing or cyclic loading is a measure of microcrack density that can be tracked with a single variable. This assumption also implies that the quasi-static cohesive law, which describes tearing, is also the envelope of the fatigue damage. This assumption is similar to the one that allows a cohesive model written in terms of a single damage variable to predict any mixed-mode path: partial damage incurred in one mode of fracture results in an equal damage in the other modes of fracture. Furthermore, the cohesive laws in each mode are assumed to be unaffected by the path of the damage evolution and mode mixity [19].

In the proposed model, fatigue damage inside the cohesive law envelope is assumed to accumulate according to a simple two-parameter law at a rate that depends on the displacement jump. Unlike other local models of this type, the two parameters of the damage law are solved using an idealization of S-N diagrams used in engineering design.

The present report is organized as follows. In Section 2, an idealization of S-N diagrams based on estimates of the endurance limit is presented. Engineering approaches are used to account for the stress ratio R . A two-parameter damage law is presented next. The two parameters are functions of the stress ratio, and can be obtained from the corresponding S-N diagrams. In Section 3, the ability of the model to predict crack propagation rates is evaluated by examining the results of a double cantilever beam (DCB) test and a mixed-mode bending (MMB) test. Some of the analyses presented correspond to experiments, and a comparison of the analysis results to experimental values provides validation of the model. Other analyses are blind predictions designed to evaluate trends in the predicted response. Several issues are considered in the analyses, including the effects of the stress ratio R , the resistance curve, and the differences between displacement control and force control during a characterization test.

2 A Cohesive Fatigue Model Based on an Assumed S-N Diagram

The main difficulty in the use of a Paris law with cohesive elements to predict fatigue crack propagation stems from the observation that, in the presence of a process zone, the Paris law is not a local measure of propagation rate. The present work is an attempt to develop a purely local damage model for cyclic fatigue, i.e., a damage model that relies exclusively on the loading history and damage accumulation at a point of interest (an integration point) and where the propagation rate is predicted rather than imposed with the Paris law. The damage model is designed such that it is capable of reproducing the S-N diagram, i.e., the effect of cyclic load on the life of the material.

2.1 S-N Diagram for Matrix Tension

The S-N curve is one of the simplest descriptions of the failure of a material as a function of the applied cyclic load. For example, the transverse tension fatigue lives of unidirectional IM7/8552 graphite/epoxy flexure specimens oriented at 90° to the longitudinal axis are plotted in Fig. 1 [20]. The specimens were subjected to 3-point bending (3PB) and 4-point bending (4PB) at a stress ratio $R = \sigma^{min}/\sigma^{max} = 0.1$. Despite the fact that the experimental results depend on the volume of the specimen, the mode of testing, and the degree of surface polishing, the fatigue data, when normalized by the static strength, σ_c , can be approximated by a straight line. (Note: subscripts are used to identify properties of the material or model, as opposed to operating variables, identified with superscripts).

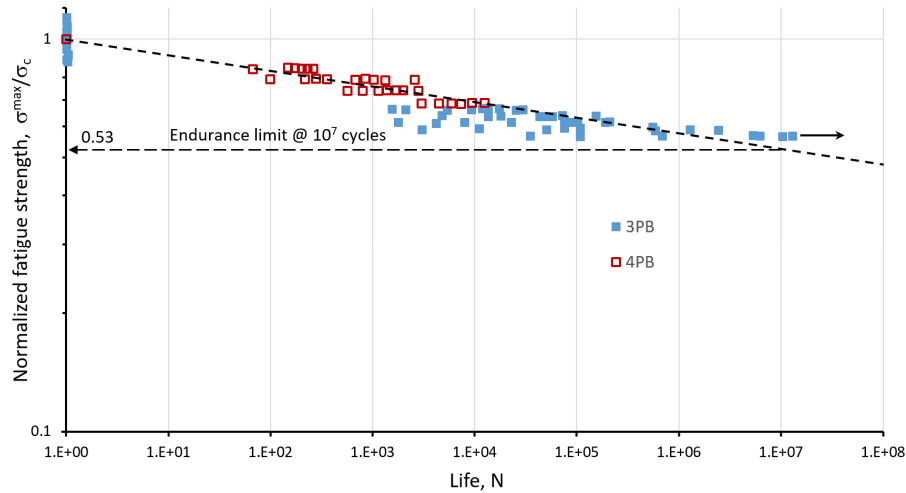


Fig. 1. S-N curve for matrix failure of IM7/8552 at $R = 0.1$ [20].

For some materials, including steels, the S-N diagram requires three lines. The first of these lines represents the low-cycle or ductile response of a material when it is subjected to high cyclic stresses. The second line represents the high-cycle response. The last line is horizontal, and it corresponds to the endurance limit cutoff below which the lives of the specimens are not affected by fatigue damage. Fleck [21] defines the endurance limit, σ_e , as the stress amplitude that a smooth unnotched sample will sustain without fracture for 10^7 cycles. The results shown in Fig. 1 suggest that a single line fits the low- and high-cycle portions of the graph, so there is no need to distinguish between the two when considering the transverse tensile loading of IM7/8552. However, the arrow next to one of the data points in Fig. 1 indicates that a runout occurred for that point. Due to the absence of data and for simplicity, no endurance cutoff was considered in the present work.

2.2 Estimating the Endurance Limit

A particularly appealing aspect of the straight line approximation of an S-N curve is that the entire curve is described by a single value: the endurance limit [2]. In addition, the endurance limit can be estimated quite easily from the material strength. As early as the 19th century, Goodman [22] observed that the endurance limit of steels subjected to fully reversed loading is approximately equal to 1/3 of the yield strength. Fleck [21] performed fatigue tests on materials including polymer

foams, elastomers, woods, polymers, composites, metallic alloys, and engineering ceramics and confirmed that the 1/3 ratio is valid for a wide range of materials. This observation is evident in Fig. 2, which was generated using the 3078 materials in the complete CES Selector material library [23].

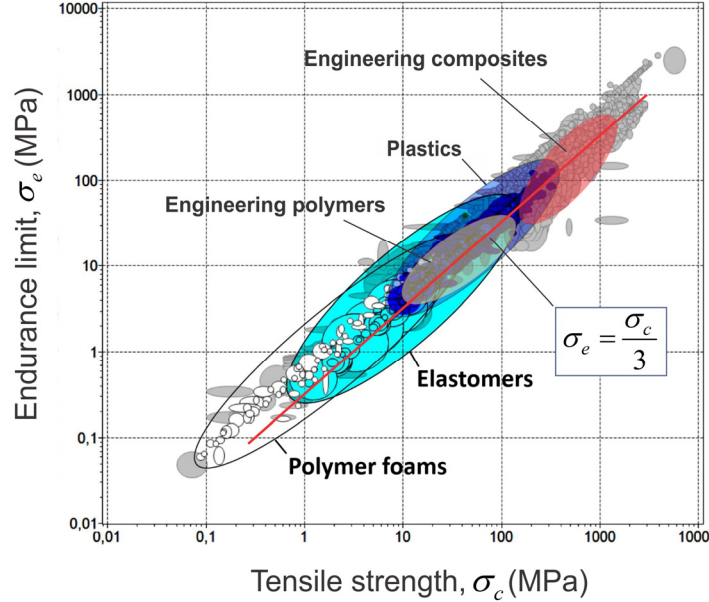


Fig. 2. Endurance limit vs. tensile strength [chart courtesy of Stéphane Gorsse, ICMCB-CNRS and Bordeaux INP, France; property chart generated with the CES Edupack, Granta Design].

2.3 Effect of Stress Ratio R on Endurance Limit

The endurance limit is usually measured using a rotating-beam specimen that subjects the material sample to a full reversal of the load ($R = -1$). A procedure to estimate the endurance limit for other values of the stress ratio is as follows. Consider the cyclic loading illustrated in Fig. 3, where R is greater than zero.

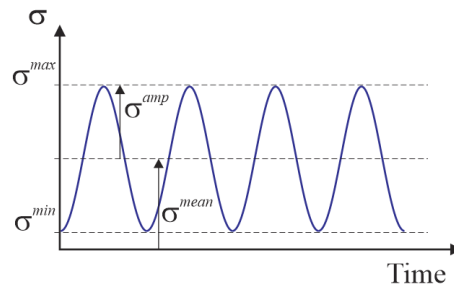


Fig. 3. Cyclic loading.

The stress amplitude σ^{amp} and the mean stress σ^{mean} can be written in terms of the stress ratio R as:

$$\sigma^{amp} = \sigma^{max} \frac{1-R}{2} \quad \sigma^{mean} = \sigma^{max} \frac{1+R}{2} \quad (3)$$

The Goodman diagram [22], a plot of alternating versus mean stress, is a design tool that represents the locus of stress states corresponding to a runout stress or a given number of cycles to failure, for example, 10^7 . The Goodman model postulates a straight line connecting the endurance limit, σ_e , on the y-axis with the ultimate stress, σ_c , on the x-axis, as shown in Fig. 4. The allowable stress amplitude σ^{amp} is then defined as a function of σ^{mean} as

$$\sigma^{amp} = \sigma_e \left(1 - \frac{\sigma^{mean}}{\sigma_c} \right) \quad (4)$$

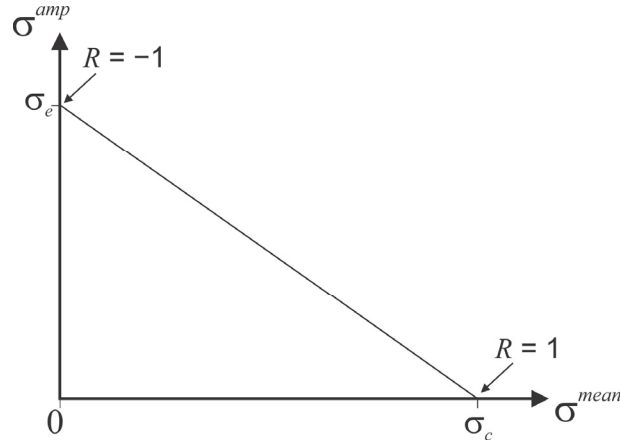


Fig. 4. Goodman diagram.

The endurance $\sigma_{eR} = \sigma^{max}$ is defined as the maximum stress for a stress ratio R that satisfies the Goodman relation. The endurance is then obtained by substituting Eq. 3 into Eq. 4:

$$\sigma_{eR} \left(\frac{1-R}{2} + \frac{1-R}{2} \frac{\sigma_e}{\sigma_c} \right) = \sigma_e \quad (5)$$

Substituting Fleck's [21] expression $\sigma_e = \frac{1}{3} \sigma_c$ into Eq. 5 gives the endurance as a function of the stress ratio R :

$$\sigma_{eR} = \frac{\sigma_c}{2-R} \quad (6)$$

Table 1 reports values of the endurance calculated from Eq. 6 for several typical values of R . It can be observed that the endurance for $R = 0.1$ is $\sigma_{eR} = 0.53 \sigma_c$. This value is consistent with the endurance used to fit the data in Fig. 1.

In summary, the present model relies on Eq. 6 and the assumption of linearity of an S-N log-log plot to establish the S-N diagram for any material and stress ratio.

Table 1. Endurance as a function of stress ratio R .

R	σ_{eR}
-1	$\frac{1}{3}\sigma_c (= \sigma_e)$
0	$\frac{1}{2}\sigma_c$
0.1	$0.53\sigma_c$
0.5	$\frac{2}{3}\sigma_c$

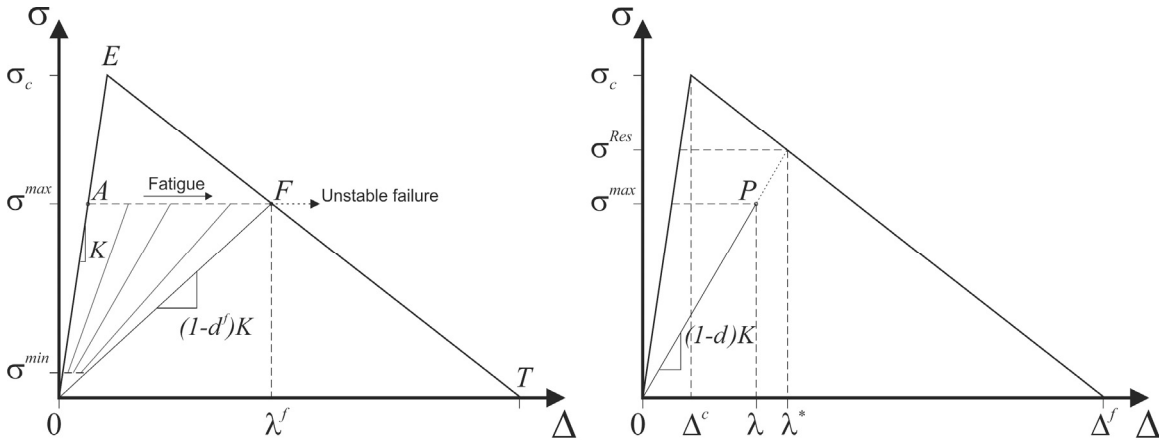
2.4 Cohesive Fatigue Damage Model

Consider an unnotched bar subjected to tensile cyclic loads, as shown in Fig. 5. A fatigue crack is assumed to occur at the center of the bar. The two-piece failure of the bar can be assumed to occur after N^f of cycles, which depends on σ^{max} and the life specified by the S-N diagram.



Fig. 5. Unnotched bar subjected to cyclic loads.

A bilinear cohesive fatigue law is illustrated in Fig. 6a. The outline of the cohesive law is composed of an elastic range $O-E$, followed by the “tearing” curve, $E-T$. Since any point outside of the cohesive outline corresponds to a failed material state, the outline represents the envelope of the damage process.



a) Description of fatigue under $\sigma^{max} = \text{constant}$.

b) Definition of displacement jumps in fatigue.

Fig. 6. Cohesive law with fatigue damage – definition of failure envelope and variables.

When σ^{max} is less than the strength σ^c , the material damages in fatigue without ever traversing the portion $A-E-F$ of the cohesive law. Instead, at any point P (Fig. 6b) damage d accumulates with the number of cycles. Consequently, the maximum displacement jump λ increases gradually from point A to point F . At point F , σ^{max} exceeds the load-carrying ability of the material defined by the tearing portion $E-T$ of the cohesive envelope and unstable failure ensues.

The evolution of fatigue damage is an unknown function of the applied cyclic load and the damage state. Heuristic power-laws of the damage increment have been proposed and justified by invoking concepts of self-similarity, where the exponent β can be seen as a stress-amplification exponent [24]. In the present work, a damage increment of the following form was investigated:

$$\frac{dd}{dN} = f(\lambda^\beta) \quad (7)$$

Several forms of the function in Eq. 7 were investigated. A final model was selected based on its ability to reproduce the S-N diagram, the ease of obtaining the required material constants, and the independence of the results from the cohesive penalty stiffness. In addition, the form of the damage accumulation model was selected for the ability of the model to predict the Paris law propagation rates, as will be described later in this paper. The following two-parameter heuristic fatigue damage accumulation model is proposed:

$$\frac{dD}{dN} = (D + \gamma) \left(\frac{\lambda}{\lambda^*} \right)^\beta \quad (8)$$

where the damage norm D is defined as [9]:

$$D = \frac{\lambda^* - \Delta^c}{\Delta^f - \Delta^c} \quad (9)$$

and where the relative displacement jump at any point P is

$$\frac{\lambda}{\lambda^*} = \frac{\sigma^{max}}{(1-D)\sigma_c} \quad (10)$$

The damage norm D can be interpreted as the ratio of the energy dissipated during the damage process over the critical energy release rate. Consequently, D is also the ratio of the damaged area over the area associated with the local discretization [9]. The norm D is a linear function of λ^* and D is also independent of the penalty stiffness. The loss of stiffness $(1-d)$ of the cohesive law is related to D as follows:

$$1 - d = \frac{\lambda^* - \Delta^f D}{\lambda^*} \quad (11)$$

For the one-dimensional constant-amplitude problem considered in Fig. 5, the total number of cycles from A to unstable failure (point F in Fig. 6a) can be calculated by integrating Eq. 8 for the range of damage $D = 0$ to D^F . The result is:

$$N^f = \left(\frac{\sigma_c}{\sigma^{\max}} \right)^\beta \int_0^{D^F} \frac{(1-D)^{-\beta}}{D+\gamma} dD \quad (12)$$

where D^F is the damage at point F (Fig. 6a):

$$D^F = 1 - \frac{\sigma^{\max}}{\sigma_c} \quad (13)$$

Eq. 12, which represents the number of cycles to failure under a constant amplitude cyclic load in terms of the maximum stress ratio, σ^{\max} / σ_c , has the form of the Basquin law of fatigue [25] times an integral term that is approximately constant for stress ratios below 95%. The results of Eq. 12 for a range of stress ratios are illustrated in Fig. 7. For stress ratios below 95%, the result of Eq. 12 is the straight line shown in black. At approximately 4 cycles, there is a knee in the curve that corresponds to the end of the low-cycle range. The parameters of the black line were chosen to fit a desired S-N curve. The plateau that characterizes the low-cycle range is chosen to be short. The effect of β , and γ on the S-N curve is illustrated by the curves obtained by perturbing β or γ from the reference solution. The coefficient γ shifts the line horizontally, while β establishes the slope of the line. Consequently, the pair of coefficients β , γ that defines the damage model in Eq. 8 can be determined by fitting the results of Eq. 12 onto an S-N curve. The next section outlines the procedure to determine these coefficients.

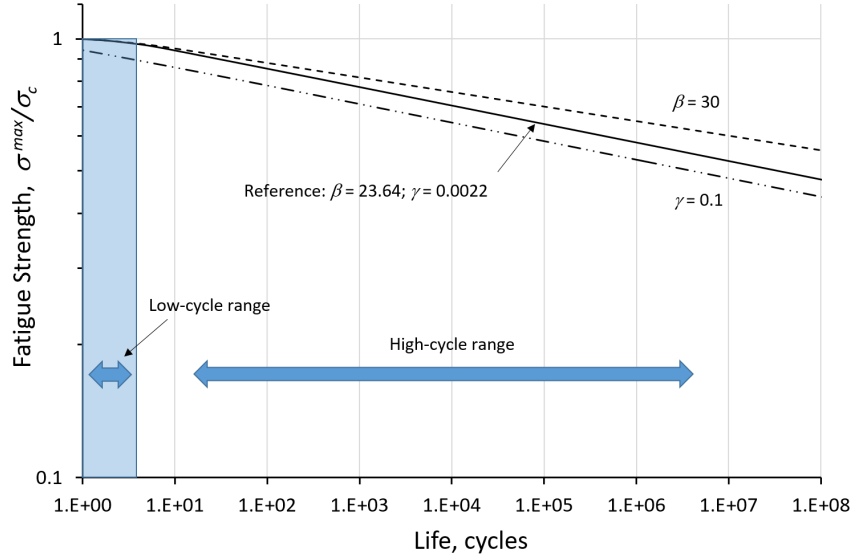


Fig. 7. Effect of β and γ on the cycles to failure obtained using Eq. 12.

2.5 Determination of Coefficients β and γ for IM7/8552

The coefficients $\beta(R)$ and $\gamma(R)$ are functions of the stress ratio R . They are calculated by fitting the curves obtained by the integral in Eq. 12 to the S-N curve of the corresponding stress ratio. The fitting is achieved by specifying two anchor points. The first point corresponds to a high maximum stress ratio that represents the end of the low-cycle fatigue portion of the S-N curve. In ductile materials, the range between the first cycle and the first anchor point can be significant. In the

present study, this point is arbitrarily set equal to two cycles, which translates into a short ductile range that appears to fit data shown in Fig. 1 well. The second anchor point is set by the endurance limit, which is calculated with Eq. 6 and reported in Table 1. The anchor points that were selected are summarized in Table 2. The calculation of the constants β and γ involves the solution of a nonlinear system of two equations for the range of stress ratios R . A simple computer program that performs this calculation is described in the Appendix.

Table 2. Anchor points defining S-N curve.

	σ^{\max} / σ_c	N^f (cycles)
Low cycle limit	0.99	2
Endurance point	σ_{eR}	1.E7

The coefficients β and γ for several typical stress ratios are reported in Table 3, and the corresponding S-N curves are shown in Fig. 8. The curve for $R = 0.1$ is darker than those for other stress ratios to highlight the fact that the test data, also shown, corresponds to this stress ratio.

Finally, it is important to emphasize that the coefficients ($\beta; \gamma$) can be determined by fitting the results of Eq. 12 to experimental data. However, in the present work, they are calculated based on the endurance limits estimated with the use of Eq. 6 and the anchor points proposed in Table 2.

Table 3. Coefficients ($\beta; \gamma$) for several values of the stress ratio.

R	β	γ
-1	13.611	0.001911
0	21.842	0.002142
0.1	23.649	0.002194
0.5	38.033	0.002643

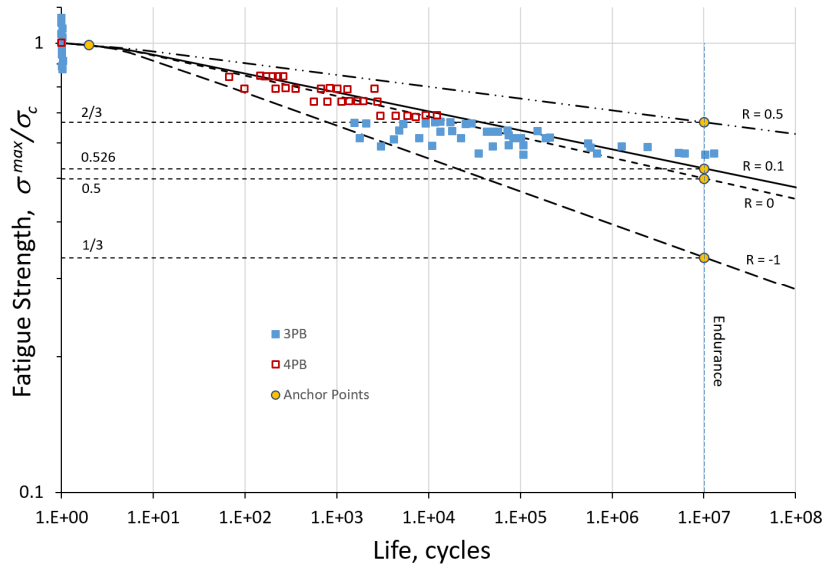


Fig. 8. S-N curves for different stress ratios obtained using Eq. 12 and the coefficients in Table 3. The test data shown by the symbols is for $R = 0.1$.

2.6 Residual Strength

The residual strength, or the strength of the material after a certain number of fatigue cycles, can also be obtained from the present model. It can be observed in Fig. 6b that the normalized residual strength is

$$\frac{\sigma^{\text{Res}}}{\sigma^{\text{max}}} = \frac{\lambda^*}{\lambda} \quad (14)$$

This ratio can be calculated as a function of damage D using Eq. 10. The number of cycles as a function of damage can be obtained for a given $\sigma^{\text{max}}/\sigma_c$ with Eq. 12. The results of an example for $R = 0.1$ are shown in Fig. 9, where the dashed lines correspond to the residual strengths for $\sigma^{\text{max}}/\sigma_c = 0.9, 0.8,$ and 0.6 . The residual strength curves terminate at the S-N line (blue curve). It can be observed that most of the loss of strength is predicted to occur rapidly near the end of the life of the material. For example, the life for a stress ratio of $\sigma^{\text{max}}/\sigma_c = 0.6$ is 459 kcycles. The predicted residual strength after 422 kcycles is still 95% of the pristine strength.

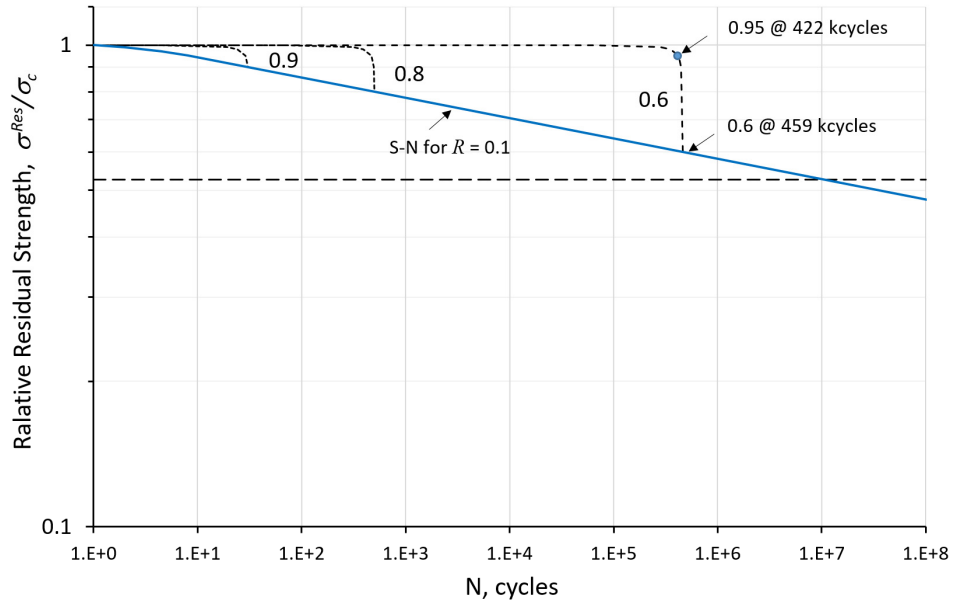


Fig. 9. Residual strength $\sigma^{\text{Res}}(N)$ for $\sigma^{\text{max}}/\sigma_c = 0.9, 0.8,$ and $0.6,$ and $R = 0.1.$

2.7 Mixed Mode

The cohesive model used herein is based on the mixed-mode model proposed by Turon et al. [26]. The primary feature of Turon's model is the manner in which the model addresses the inaccuracies that can occur in predicting mixed mode delamination propagation with cohesive zone models. The model establishes an interdependence between the mode I and mode II model parameters. Using a rigorous mathematical framework, Turon demonstrated that a necessary condition for thermodynamic consistency is that the ratio Δ^c / Δ^I must be constant during the analysis for all mode mixities [26]. Consequently, Turon's model imposes the following constraint:

$$\frac{\Delta^c}{\Delta^f} = \frac{\sigma_c^2}{2K_I G_{Ic}} = \frac{\tau_c^2}{2K_{sh} G_{IIc}} \quad (15)$$

where G_{Ic} and G_{IIc} are the critical ERR for modes I and II, respectively, σ_c and τ_c are the interlaminar peel and shear strengths, and K_I and K_{sh} are the penalty stiffnesses in mode I and in mode II. The constraint represented by Eq. 15 is imposed by selecting the value of the K_{sh} penalty stiffness that satisfies the identity.

As all cohesive models based on the Dávila-Camanho formulation [19], Turon's mixed mode cohesive law is bilinear. The law consists of a continuous sweep between mode I and mode II. In mixed mode, the law is defined by the effective mixed-mode displacements jumps λ , Δ^c and Δ^f , and the penalty stiffness, K_B . The effective mixed-mode displacement jump is defined as [26]

$$\lambda = \frac{K_{sh} (\lambda_1^2 + \lambda_2^2) + K_I^2 \langle \lambda_3 \rangle^2}{\sqrt{K_{sh}^2 (\lambda_1^2 + \lambda_2^2) + K_I^2 \langle \lambda_3 \rangle^2}} \quad (16)$$

where λ_1 and λ_2 are the orthogonal in-plane displacement jumps and λ_3 is the opening displacement jump. The penalty stiffness in mixed mode is

$$K_B = \frac{K_{sh}^2 (\lambda_1^2 + \lambda_2^2) + K_I^2 \langle \lambda_3 \rangle^2}{K_{sh} (\lambda_1^2 + \lambda_2^2) + K_I \langle \lambda_3 \rangle^2} \quad (17)$$

and the local mixed-mode ratio is defined as:

$$B = \frac{K_{sh} (\lambda_1^2 + \lambda_2^2)}{K_{sh} (\lambda_1^2 + \lambda_2^2) + K_I \langle \lambda_3 \rangle^2} \quad (18)$$

Finally, Turon's model defines the critical displacements Δ^c and Δ^f as

$$\Delta^c = \frac{\sqrt{\frac{\sigma_c^2}{K_I} + \left(\frac{\tau_c^2}{K_{sh}} - \frac{\sigma_c^2}{K_I} \right) B^\eta}}{\sqrt{K}} \quad \text{and} \quad \Delta^f = \Delta^c \frac{2K_I G_{Ic}}{\sigma_c^2} \quad (19)$$

where η is the coefficient of the Benzeggagh-Kenane mixed-mode fracture criterion:

$$G_c = G_{Ic} + (G_{Ic} - G_{IIc}) B^\eta \quad (20)$$

To apply the fatigue model defined in the previous section to mixed mode, the S-N diagram must be corrected for the difference between axial and shear loading. Juvinal [1] suggests correcting the endurance limit with the following load correction factor:

$$C_L = \begin{cases} 1 & \text{axial and bending} \\ 0.58 & \text{shear (torsion)} \end{cases} \quad (21)$$

To account for variable mode mixity in delamination, the following linear interpolation of the load correction factor is proposed:

$$C_L = 1 - 0.42 B \quad (22)$$

The endurance limit for mixed mode is then estimated to be

$$\sigma_{eR_mixed} = C_L \sigma_{eR} = (1 - 0.42 B) \frac{\sigma_c}{2 - R} \quad (23)$$

The coefficients β and γ of the damage model can be calculated and tabulated in terms of the stress ratio R and the mode mixity, B . Alternatively, the combined effect of R and B on the endurance limit can be accounted for with a single variable by defining an effective stress ratio, R^{eff} , such that:

$$\sigma_{eR_mixed} = (1 - 0.42 B) \frac{\sigma_c}{2 - R} = \frac{\sigma_c}{2 - R^{eff}} \quad (24)$$

Solving for R^{eff} gives:

$$R^{eff} = \frac{R - 2}{1 - 0.42 B} + 2 \quad (25)$$

The values of $\beta(R)$ and $\gamma(R)$ reported in Table 3 can be used in mixed mode by substituting R^{eff} for R . Only positive stress ratios R are considered here because negative stress ratios in mixed mode require additional considerations to counter the effect of closing displacements on crack propagation. However, the range of the effective stress ratio corresponding to positive stress ratios R is $-1.45 < R^{eff} < 1$, as can be observed in Fig. 10. In the constitutive subroutine of the damage model, the values of $\beta(R^{eff})$ and $\gamma(R^{eff})$ are tabulated and intermediate values are calculated with a linear interpolation procedure.

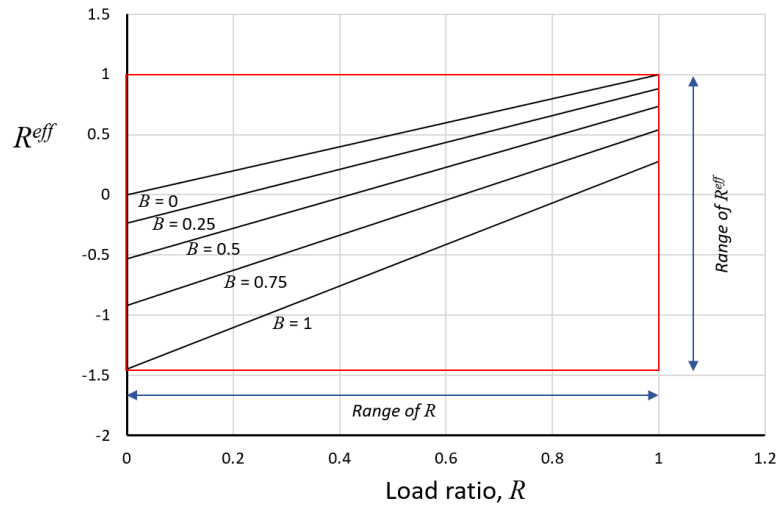


Fig. 10. Plot of R^{eff} as a function of stress ratio R for mode mixities ranging from 0 to 1.

2.8 Predicting Crack Propagation with Simplified Cyclic Loading (SCL)

The cohesive fatigue model proposed in Eq. 8 and the determination of the coefficients β and γ described in the previous section are based on the assumption that damage, i.e., a measure of microcrack density and loss of stiffness at a material point, characterizes simultaneously a degradation of the material by fatigue or by partial tearing. In other words, the model assumes that both states of damage evolve together such that a reduction in remaining life is always accompanied with a degradation of the tearing resistance and vice-versa. This assumption ensures that the envelope of the cohesive law is valid for tearing, for fatigue, or for any combination of the two so that a single variable, d , is sufficient to track the effects of all aspects of the past loading history at a material point. Therefore, the model is notionally capable of accounting for damage accumulation anywhere within the cohesive envelope. Although the model coefficients are determined from the constant maximum stress conditions of an S-N diagram, the model can capture the fatigue damage accumulation along any loading path in the same manner that Miner's rule [1] can be used with the S-N diagram to accumulate damage from different cyclic loading conditions.

The fatigue damage model was implemented in a finite element framework as a cohesive constitutive model and solved within a simplified cyclic loading (SCL) procedure that avoids the computational expense of having to cycle the applied load. In SCL, the maximum load is held constant. For simplicity, the frequency of cyclic loading is 1 Hz, so that the analysis pseudo-time represents the number of cycles, as illustrated in Fig. 11. The effect of cycling on fatigue damage is represented by the stress ratio R within the constitutive damage model. The analysis is conducted in two steps. The first step from 0 to 1 introduces the applied load (force or displacement). No fatigue damage is allowed in the first step. During the second step, the applied load is held constant but the solution is recalculated to account for the internal load redistribution that occurs with fatigue and tearing damage accumulation.

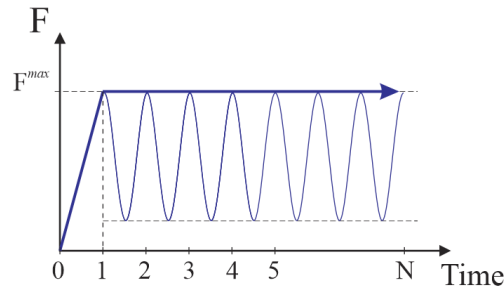


Fig. 11. SCL procedure: the load is held constant during the analysis while the effects of loading amplitude, stress ratio, cycle count, and damage accumulation are processed within the constitutive model.

A user-written UMAT subroutine for Abaqus cohesive elements was developed. UMAT subroutines are called by the Abaqus implicit solver at every integration point, at every equilibrium iteration of every time increment. The subroutine receives the current damage state, the displacement jump, and the analysis time increment. The output of the subroutine is the damage state. A UMAT for fatigue damage was written by modifying a UMAT of Turon's quasi-static cohesive model [26]. Implementation of the fatigue model within the quasi-static cohesive UMAT

only required adding the calculation of the fatigue damage, which was achieved with the few lines illustrated in Fig. 12.

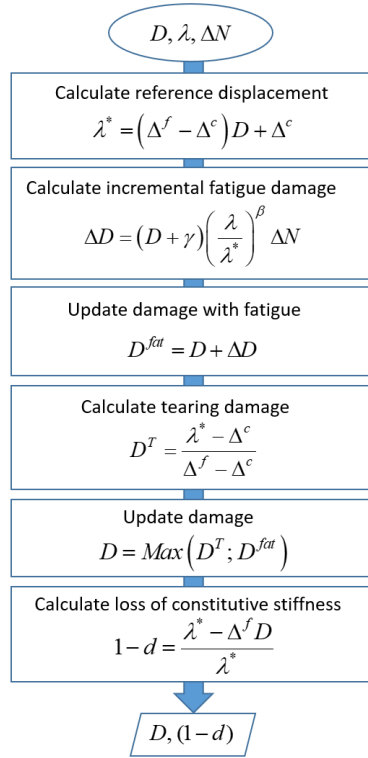


Fig. 12. Calculation of damage accumulation using the SCL procedure.

3 Validation: Crack Propagation in Mode I and Mixed Mode

3.1 Analysis of Double Cantilever Beam Specimen

The double cantilevered beam (DCB) specimen is a standardized test method for determining the onset of delamination propagation [27]. The DCB specimen has also been used for determining the delamination growth rate in fatigue [28, 29]. The results of an extensive characterization of delamination onset and growth under Mode I fatigue loading of IM7/8552 graphite/epoxy unidirectional tape specimens by Murri [28] were used in the present study to evaluate the ability of the proposed model to predict delamination propagation rates.

3.1.1 Finite Element Model of DCB Specimen

The DCB specimens tested by Murri were manufactured with 24 plies of IM7/8552 unidirectional tape with a thin Teflon film at the mid-plane at one end to induce an initial delamination. The specimens were nominally 178-mm long and 25.4-mm wide. The configuration of the test specimen is defined by the nominal dimensions reported in Table 3.

The parametric model of a DCB specimen shown in Fig. 13 was constructed in Abaqus/Std [4]. The model parameters can be used to change the dimensions of the specimen and the number of

elements in each of the regions of the model. For computational efficiency, the width of the model is 1 mm and the reaction force is scaled by the width $b = 25.4$ mm of the specimen. The propagation zone length varied between 5 mm and 15 mm, depending on the length of crack propagation that was needed. To ensure accurate trends in the crack propagation rates, the element edge length in the propagation zone of the model is 0.04 mm. A mesh convergence study indicated that an element size up to 0.1 mm is sufficient to predict crack length as a function of cycles, but the propagation rate becomes noisy. Three layers of SC8R continuum shell elements were used through the thickness of each arm, and three elements were used across the width. The material properties used in the analysis are provided in Table 4, and were generated within the scope of the NASA Advanced Composites Project [30].

Table 3. Dimensions of DCB specimen in mm.

a_0	b	h
50.8	25.4	2.25

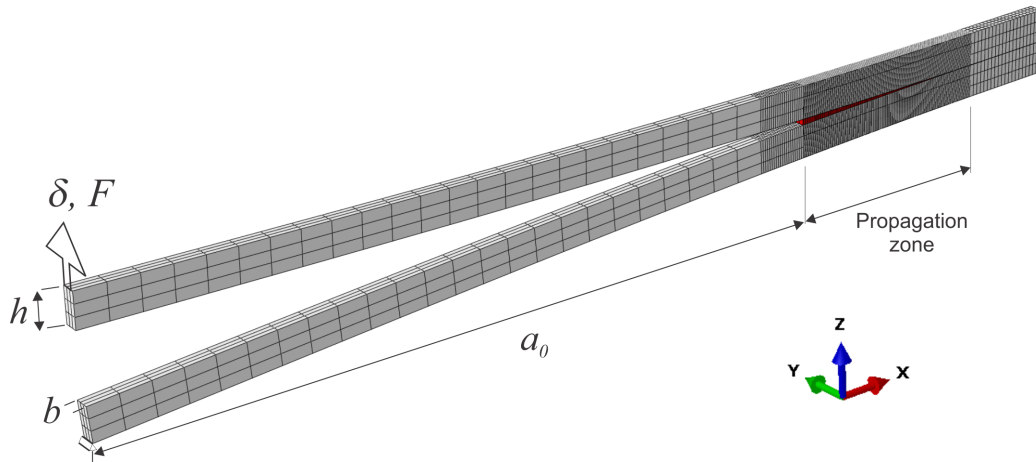


Fig. 13. Finite element model of a 1-mm-wide strip of a DCB specimen.

Table 4. Material properties of IM7/8552 [30].

E_{11} (avg T/C)	146,671.	MPa
$E_{22}=E_{33}$	8703.	MPa
$G_{12}=G_{13}$	5164.	MPa
G_{23}	3001.	MPa
G_{Ic}	0.240	N-mm/mm ²
G_{IIc}	0.739	N-mm/mm ²
σ_c	80.1	MPa
τ_c	97.6	MPa
η	2.1	

To simulate the experimental procedure, which was conducted under displacement control, the model was loaded with a constant applied displacement δ , and the reaction force, F , was recorded as a function of the number of cycles.

3.1.2 Predicting Paris Law Propagation Rate

The crack length, a , can be obtained by direct examination of the finite element model at repeated cycle increments, although such post-processing can be tedious. Alternatively, the crack length can be calculated from the compliance $C = \delta/F$ of the model using a closed form expression derived by the corrected beam theory. Written in terms of the compliance, the crack length is [31]

$$a = \left(\frac{3}{2} C EI \right)^{\frac{1}{3}} - \chi h \quad (26)$$

where

$$EI = E_{11} \frac{bh^3}{12}; \quad \chi = \sqrt{\frac{E_{11}}{11G_{13}} \left[3 - 2 \left(\frac{\Gamma}{1+\Gamma} \right)^2 \right]} \quad \text{and} \quad \Gamma = 1.18 \frac{\sqrt{E_{11}E_{22}}}{G_{13}} \quad (27)$$

and the ERR during the simulation varies as a function of the reaction force F and the crack length a according to

$$G_I = \frac{F^2 (a + \chi h)^2}{b EI} \quad (28)$$

The analyses were performed with applied displacements $\delta_{\max} = 1.48$ mm, 1.7 mm, 1.92 mm, and 2.25 mm. At the start of the analyses, these displacements correspond to G/G_{Ic} ratios of 0.3, 0.4, 0.5, and 0.69, respectively. As the cracks propagate, these ratios become smaller. The rates of propagation were obtained by calculating $\Delta a/\Delta N$ from the crack lengths obtained using Eq. 26. The analysis results and the corresponding experimental values are shown in Fig. 14. The arrows indicate the direction of progression, from the start towards the end of the simulations. The blue circular symbols shown on the predicted curves in Fig. 14 correspond to a 5% increase in specimen compliance compared to the compliance at the start of the simulation. This change occurs after 0.9 mm of delamination propagation. This point is sometimes referred to as the 5% onset [32].

The predicted propagation rates start high and then quickly reduce to a rate that falls onto the straight line of a Paris law. The initial transient response is the result of the formation of a process zone, which starts with the tearing damage caused by the first loading cycle, and then grows under the cyclic loading to a stable size. The band of red elements in Fig. 15a correspond to the process zone. The elements to the left of the process zone are completely damaged, and those to the right are intact. The crack extension as a function of the number of cycles is reported in Fig. 15b. The points correspond to lengths of propagation measured from the analysis results in Fig. 15a, and the curve was obtained using the compliance solution given by Eq. 26. Both methods provide similar results, but the compliance method is much easier to generate.

At steady-state propagation, the l_{pz} is observed to be approximately 0.3 mm, and it remains constant during propagation despite the fact that the ERR and the corresponding crack propagation

rate decrease with crack length. In fact, the length of the process zone appears to be independent of the applied cyclic load and nearly identical to the 0.35 mm that forms by quasi-static tearing.

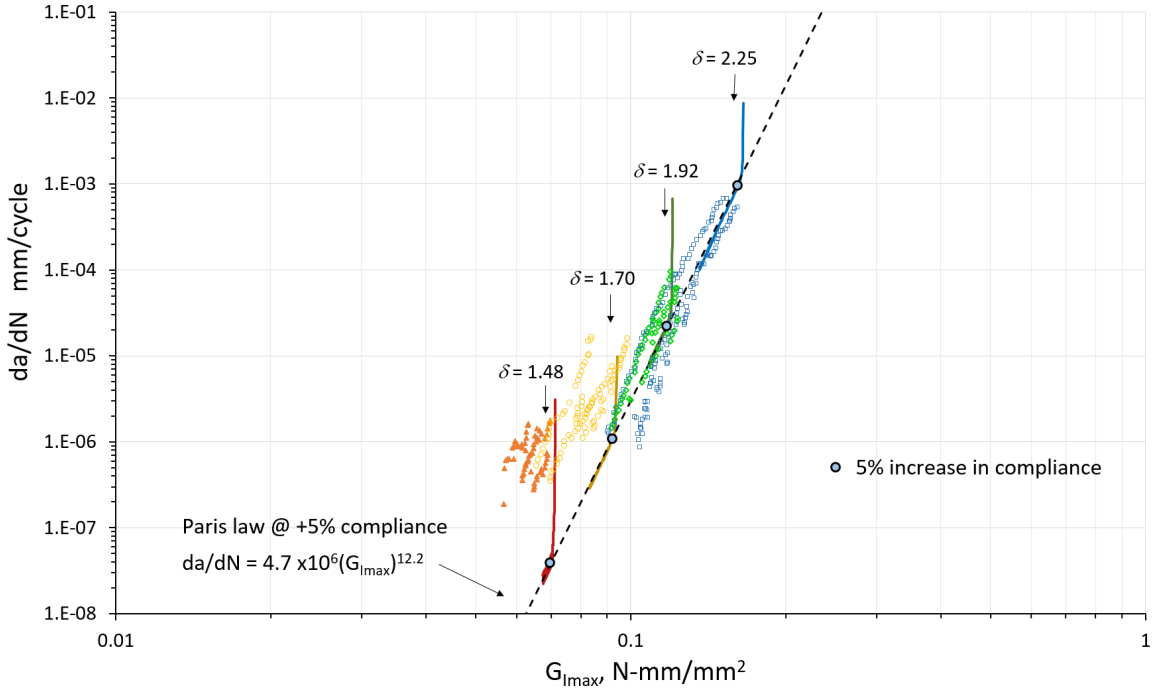


Fig. 14. Comparison of measured and predicted delamination growth rates in a DCB specimen for different values of the applied displacement.

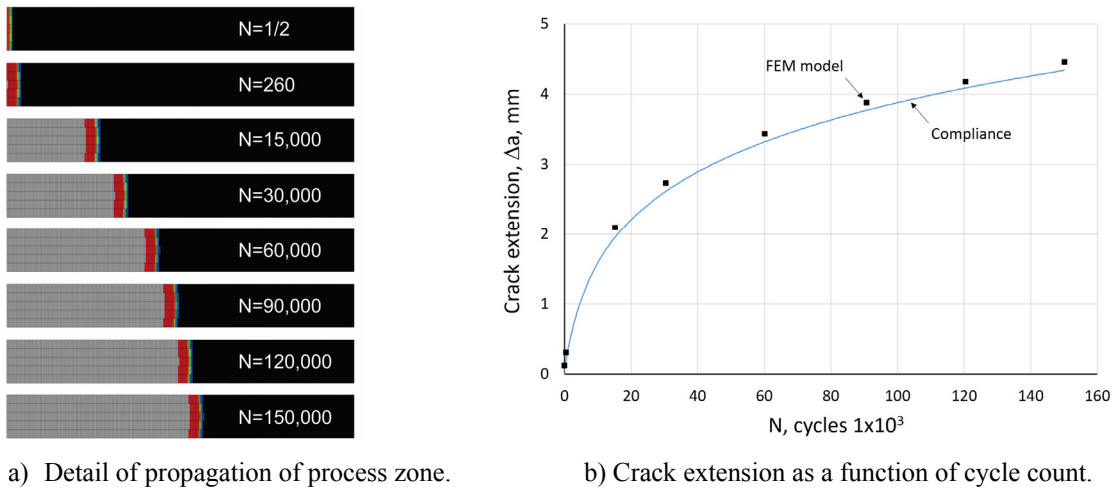


Fig. 15. Crack propagation in DCB specimen with applied displacement $\delta_{\text{max}} = 1.92$ mm.

The rate of convergence of the iterative solution of equilibrium in the presence of damage is always an issue in implicit finite element analyses. Damage often causes local instabilities that may prevent convergence of the solution. In the case of fatigue analyses with the SCL loading procedure, the propagation is gradual and no convergence issues were encountered. When the analysis is

allowed to set automatically the time increment, the increment increases when the number of iterations required to achieve convergence is small, and the increment decreases when the procedure fails to converge in a prescribed number of iterations. However, the time increments were generally extremely small. In the current implementation of the UMAT subroutine, the tangent stiffness of the constitutive model is calculated numerically rather than analytically by applying perturbations to the displacement jumps. In this method of calculation, changes in the fatigue damage are not taken into account. It was found that computational efficiency was gained by setting a low maximum number of cycles per increment. Time increments of more than 1300 cycles/mm (about 40 cycles per element) converge in a single iteration, which avoids unnecessary cuts and restarts. Future work will have to address the issues that limit the convergence rate of the solution.

3.1.3 Bridging and R-curve Effects

The predicted Paris law line shown in Fig. 14 fits the average of the experimental data. However, a closer examination of the experimental data indicates that the test data is composed of lines that are shifted left or right of the Paris law, depending on the magnitude of the applied displacement. Several authors have attributed this shift to the effect of the delamination resistance curve (R-curve), which is the effective increase in the ERR as the crack propagates [28, 33]. The R-curve for IM7-8552 shown in Fig. 16 was measured by Murri [28]. For a propagation $\Delta a \leq 12.5$ mm, the R-curve can be approximated with the linear function, as shown in the figure. For $12.5 \text{ mm} \leq \Delta a \leq 22 \text{ mm}$, the R-curve can be approximated by a steady-state constant value. The data for longer crack lengths is not considered in the analysis.

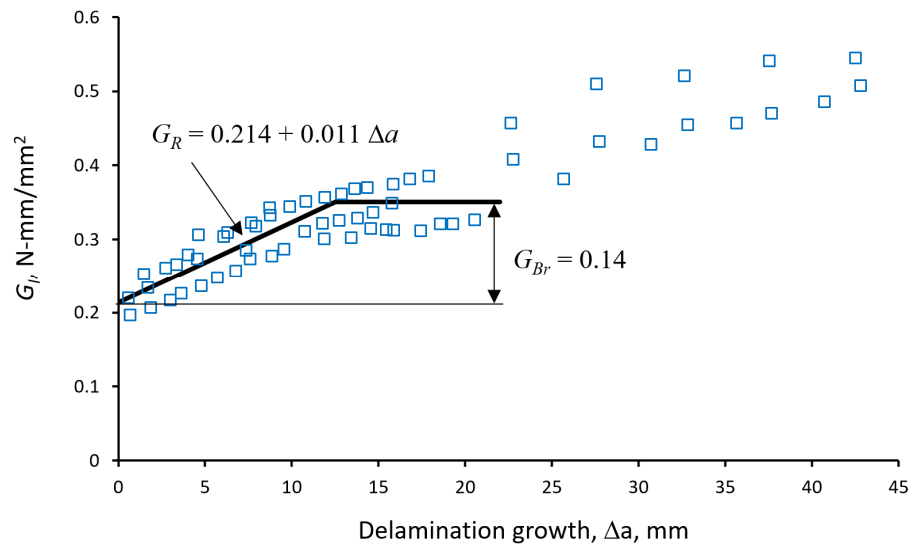


Fig. 16. Delamination resistance curve for IM7/8552 material obtained from static DCB tests [28].

Previous research by the author has shown that it is possible to represent R-curves that exhibit a steady-state plateau by superposing two bilinear cohesive laws [34]. The result of the superposition is a trilinear law, as illustrated in Fig. 17. The procedure for representing the superposed laws in a

finite element model consists of generating a duplicate set of cohesive elements that share nodes with a base layer of cohesive elements. The cohesive law of the base layer is defined by its strength σ_{c0} and maximum displacement jump Δ^{f0} . The superposed elements represent a “bridging” law defined by σ_{cBr} and Δ^{fBr} . The penalty stiffness of the bridging law is chosen such that the Δ^c for the base and the bridging laws are equal, which ensures that the sum of the two laws is trilinear rather than quadrilinear [35].

The slope of an R-curve can be represented by changing σ_{cBr} . For a given G_{Br} , smaller values of σ_{cBr} result in shallower slopes of the R-curve. Once the displacement jump at the crack tip reaches Δ^{fBr} , steady-state propagation occurs, $G_c = G_{c0} + G_{Br}$, and the R-curve becomes horizontal, as illustrated by the black line in Fig. 16. Conceptually, additional sets of cohesive elements could be added to capture a second slope of the R-curve beyond 22 mm of propagation. However, cohesive models always reach steady-state propagation after a certain length of propagation, unlike the experimental R-curve shown in Fig. 16.

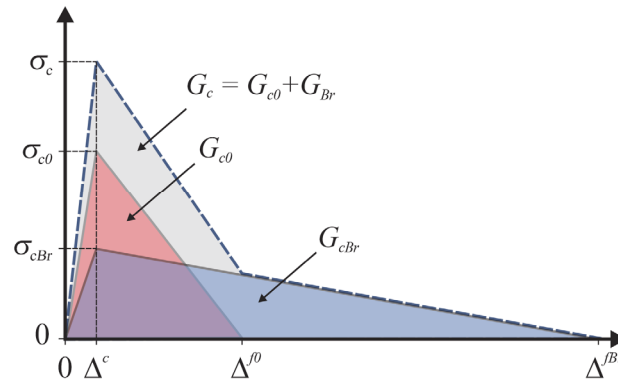


Fig. 17. Superposition of bilinear cohesive laws

A quasi-static analysis of the DCB specimen was conducted to determine the strength of the bridging law that results in a process zone of approximately 12.5 mm. The critical ERR of the base and bridging laws are 0.214 N-mm/mm² and 0.14 N-mm/mm², respectively, as shown by the curve fit on Fig. 16. By performing several quasi-static analyses, it was found that a bridging strength $\sigma_{cBr} = 0.8$ MPa resulted in the desired R-curve. The penalty stiffness of the bridging law was calculated such that the critical displacement jump Δ_c for the base and the bridging law are the same. The cohesive properties for nominal and bridge models are summarized in Table 5.

Table 5. Cohesive properties for nominal (unbridged) and bridged analysis.

		G_c (N/mm)	σ_c (MPa)	K (N/mm ³)
superposed {	Nominal	0.240	80.1	$2 \cdot 10^5$
	Base	0.214	80.1	$2 \cdot 10^5$
	Bridge	0.140	0.8	$2 \cdot 10^3$

The difference in the predicted quasi-static response of the DCB with and without bridging can be observed in the force-displacement curves shown in Fig. 18. The curve without bridging follows closely the analytical solution ($G_c = 0.24 \text{ N-mm/mm}^2$). The curve with superposed bridging starts to deviate from linearity at $G_c = 0.214 \text{ N-mm/mm}^2$, and the steady state value of the combined ERR ($G_c = 0.354 \text{ N-mm/mm}^2$) is reached after 12.5 mm of propagation, which confirms the experimental description of the R-curve provided by Murri and reported in Fig. 16.

The model with superposed cohesive elements was used to conduct fatigue analyses under displacement control using the same applied displacements $\delta_{\max} = 1.48 \text{ mm}$, 1.7 mm , 1.92 mm , and 2.25 mm as in the previous section. Three additional analyses were conducted using force control, with $F = 50.8 \text{ N}$, 73.7 N , and 80.5 N . The results are shown in Fig. 19, where the red curves correspond to the analyses conducted under displacement control, and the green curves correspond to analyses conducted under force control. The results for different applied loads do not align along a single Paris law, as they do when a bridging law is absent. Instead, the results for different applied displacements align in parallel segments that shift to the right with increasing values of the applied displacement. In addition, the results for analyses conducted under force control are non-monotonic, especially for the higher applied load of 80.5 N , where the propagation rate increases more rapidly as the ERR approaches G_c . This increase in the propagation rate is an indication that the damage model is capable of transitioning seamlessly from fatigue propagation to tearing as the ERR increases.

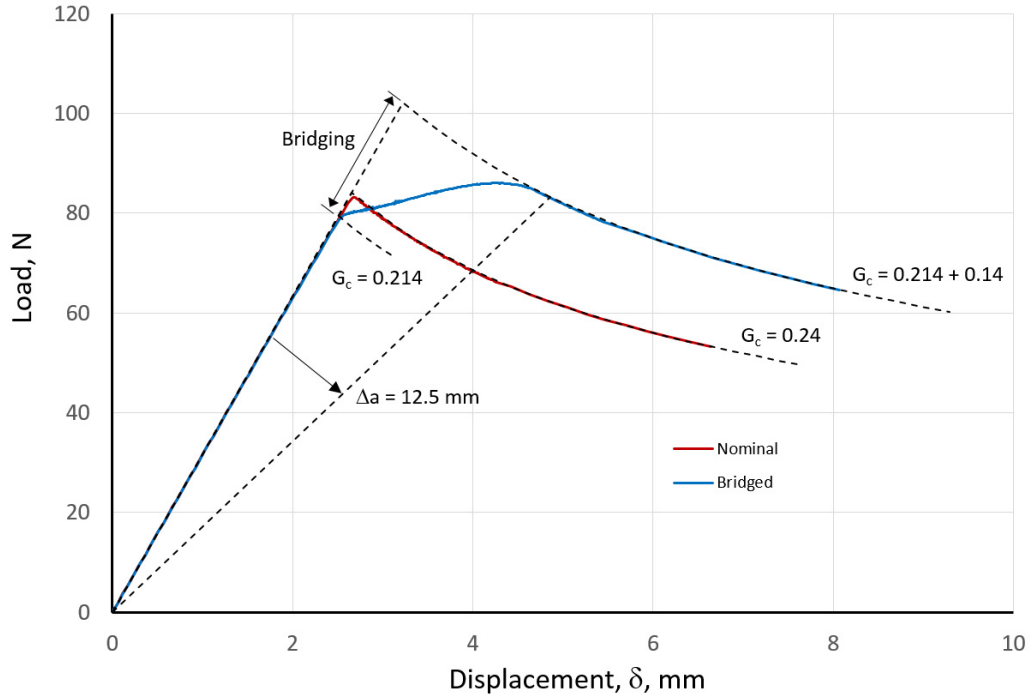


Fig. 18. Predicted force-displacement curve for DCB test: with and without bridging.

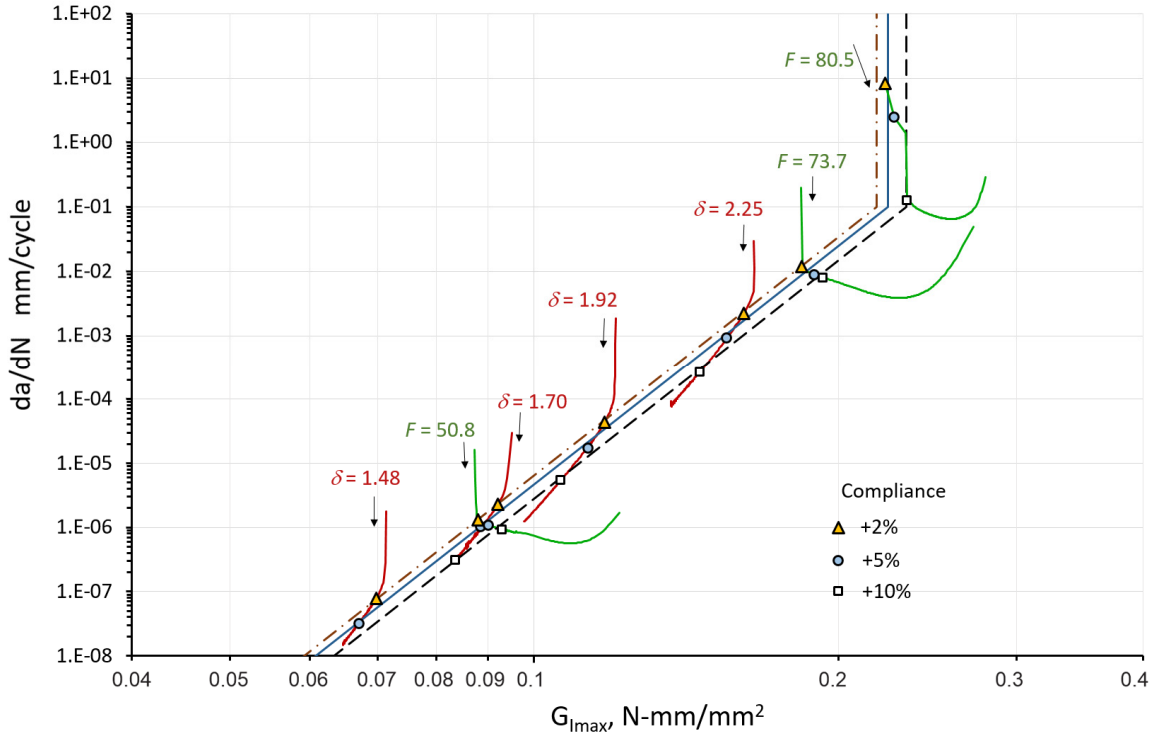


Fig. 19. Predicted delamination growth rates in a DCB specimen for different values of applied displacement (red) and applied force (green).

It is not possible to fit with a single Paris law all of the displacement control and force control analysis results in Fig. 19. However, the propagation rates at specified points do line up. The points corresponding to +2%, +5%, and +10% increases in the compliance of the specimen are shown on each analysis curve in Fig. 18. These increases in compliance correspond to propagation lengths of 0.36 mm, 0.91 mm, and 1.75 mm, respectively. The three sets of points line up along three nearly parallel Paris laws represented by the dashed lines. These dashed lines are also associated with values of G_R obtained using the equation shown in Fig. 16. They correspond to ERR of 0.218 N-mm/mm², 0.224 N-mm/mm², and 0.234 N-mm/mm², respectively. The dashed lines are drawn vertical at the point where the abscissa equals the ERR for each line to represent the transition between the fatigue propagation range and the tearing range.

For the specimen loaded with a force of 80.5 N the initial propagation is in tearing rather than fatigue. Indeed, the first 0.8 mm of propagation occur during the first cycle. The 10% compliance point is reached after two cycles, and the entire simulation ends after 67 cycles with a total propagation length of 9 mm. At the end of the analysis, the propagation rate approaches 1 mm per cycle and elements fully damage in fractions of a cycle. At such high rates, it may be unreasonable to consider fatigue damage a continuous function of time.

The analysis results conducted under displacement control and with the R-curve is included are shown again in Fig. 20 with the corresponding experimental results. A visual comparison indicates that trends predicted with an R-curve represent the experimental results better than the predictions that do not take into account the R-curve (Fig. 14).

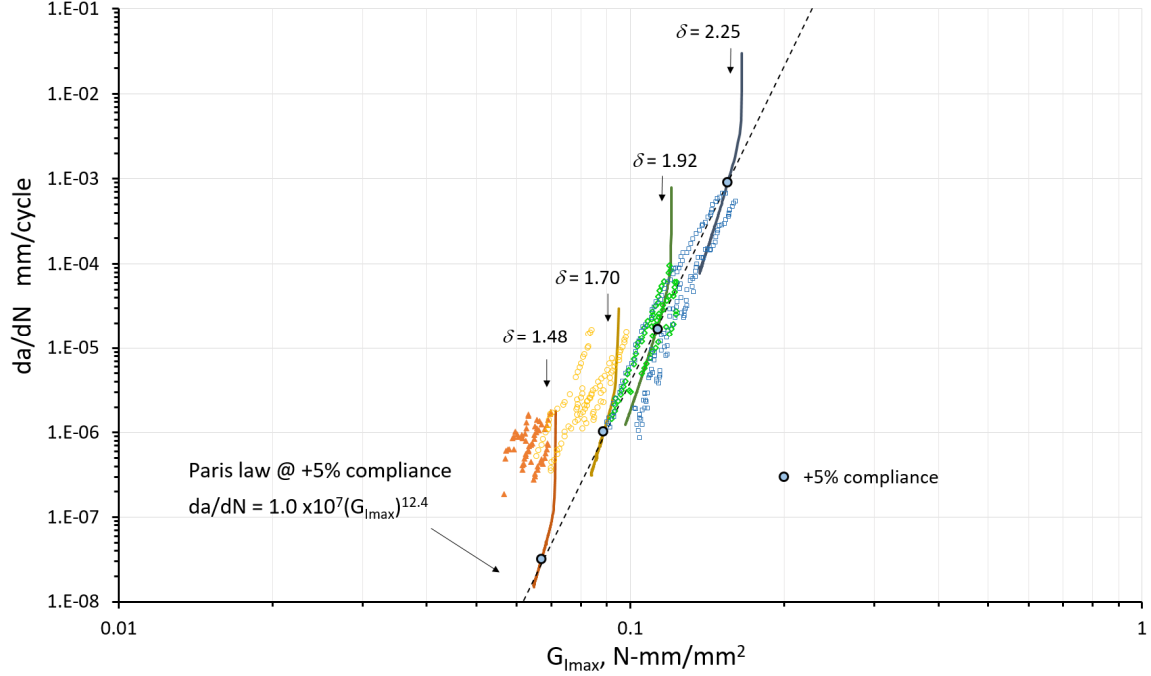


Fig. 20. Comparison of predicted delamination growth rates with R-curve bridging included with experimental results.

3.1.4 Predicting the Effect of the R Ratio on the Paris Law

The effect of the stress ratio R was investigated for $R = 0.0, 0.1,$ and 0.5 using the damage model parameters β and γ shown in Table 3. Analyses were conducted using at least two different values of the applied maximum displacement δ_{max} . The results of seven simulations are shown in Fig. 21. As in the previous section, lines representing the Paris law were fitted through the points corresponding to a 5% increase in compliance (0.9 mm of propagation). The numerical results indicate that the fitted Paris lines intersect at an abscissa of $G = 0.224$ N-mm/mm², which corresponds to the value of G_R at 0.9 mm of propagation (see R-curve in Fig. 16). The ordinate of the intersection is 0.1 mm/cycle. Several authors [17, 36, 37] have observed similar trends on the effect of the stress ratio on the Paris lines. In particular, Allegri [38] observed that the effects of stress ratio and mode mixity can be described in terms of the normalized peak ERR as rotations of the Paris line. By normalizing the ERR by the value of G_R that corresponds to any given propagation length, the predicted propagation rates for all values of R can be fitted with a single equation:

$$\frac{da}{dN} = C \left(\frac{G}{G_R} \right)^{m^*(1-R)^\rho} \quad (29)$$

with $C = 0.1$, $m^* = 11.5$, and $\rho = -0.69$. The simplicity of this equation renders it useful for extending the experimental values of the Paris law obtained at a particular R ratio to other ratios that were not tested. However, it is unclear at this time if the fact that the curves intersect at G_R is

a result of the present model, a coincidence for particular materials or, as postulated by Allegri, if it is a fundamental property of the fracture of materials.

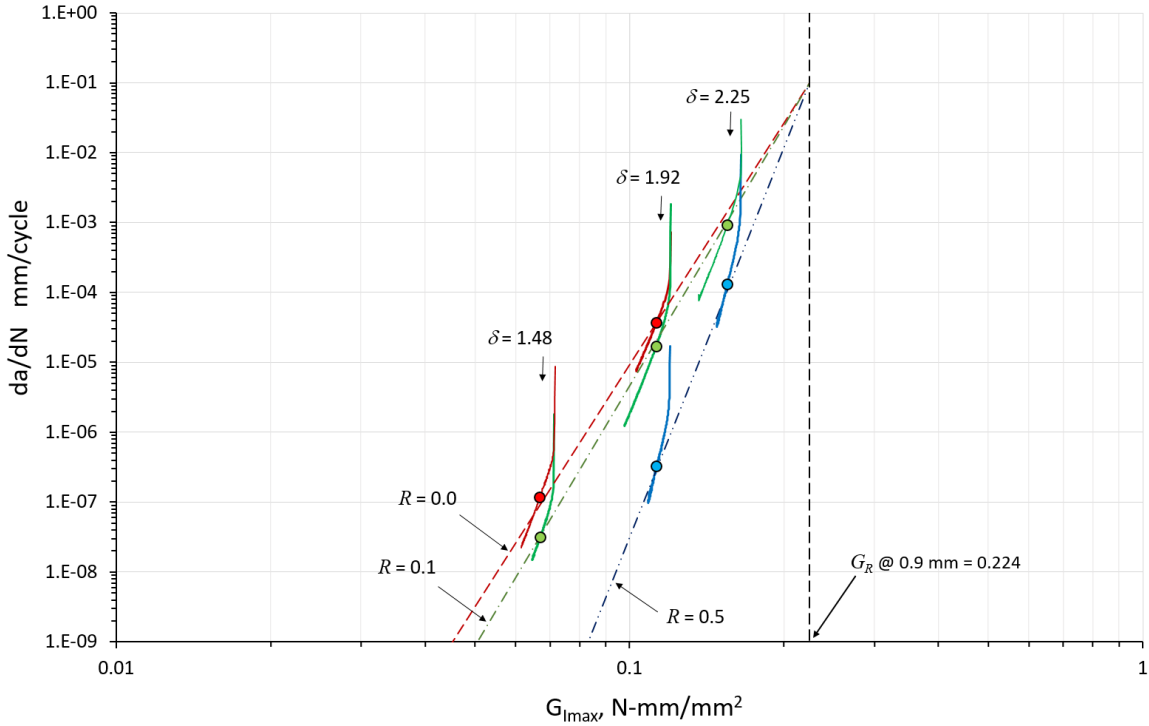


Fig. 21. Delamination growth rates for stress ratio $R = 0.0, 0.1,$ and 0.5 with $\delta_{\max} = 1.48, 1.92,$ and 2.25 mm.

Finally, the form of Eq. 29 is also consistent with the observation made in the previous section that, in the presence of an R-curve, the Paris law is a function of the length of propagation. According to Fig. 16, the ERR for the propagation lengths of 0.36, 0.91, and 1.75 mm (2, 5, and 10% compliance change) are $G_R = 0.218, 0.224,$ and 0.234 N-mm/mm², respectively. The three Paris lines shown in Fig. 19 were obtained by substituting these three values of G_R into Eq. 29 with the values of $C, m,$ and ρ already specified.

3.1.5 Analysis of Propagation Onset

As previously discussed, during the initial cycles in a fatigue simulation the front of the process zone propagates at a faster rate than when the process zone is fully developed. In a physical test, the processes that occur during initiation may be different. For instance, the initial growth of a delamination from the edge of a Teflon insert may be slower, rather than faster than subsequent growth, because of the bluntness of the initial crack tip or the presence of a resin-rich wedge at the end of the Teflon film. Yet delamination onset [32], defined as the G - N curve of the number of cycles N required to change the compliance by a specified amount for a given ERR level G , is a useful characteristic of a material interface for material selection and product design. It is therefore

interesting to investigate if the G - N curves of delamination onset predicted by the present model correlate well with the experimental results.

In Murri's characterization of delamination in IM7/8552, onset was defined as the number of cycles until the compliance increases by 5%. The analysis results were taken from the four simulations shown in Fig. 20, complemented by the point $G_{Ic} = 0.24 \text{ N-mm/mm}^2 @ 1 \text{ cycle}$. The results are shown in Fig. 22, with a blue line with white symbols representing the analysis results and the black symbols corresponding to the experimental measurements. The experimental values below 0.07 N-mm/mm^2 are runouts, i.e., the testing was interrupted before achieving onset. The model does not have the ability to predict runouts. These results indicate that the model proposed predicts well the delamination onset curve. Future versions of the present model will include thresholds to better represent the low range of the propagation rates.

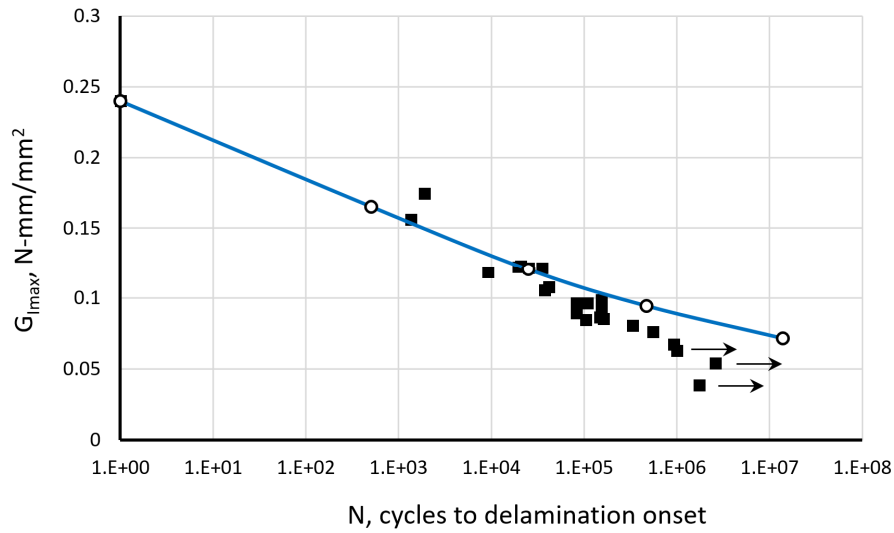


Fig. 22. Comparison of predicted and measured delamination onsets for $R = 0.1$ [28].

3.2 Analysis of the Mixed Mode Bending Test

The mixed-mode capabilities of the fatigue model proposed herein were evaluated by analyzing the mixed-mode bending (MMB) specimen tested by Ratcliffe [39]. The specimens were made with IM7/8552 tape, and they were nominally identical to the DCB specimens tested by Murri and described in Section 3. The dimensions of the specimen are listed in Table 5. A finite element model of the test configuration is shown in Fig. 23. Each arm of the model is composed of three layers of SC8R continuum shell elements. Five rows of elements were used across the width. In the propagation zone of the model, the mesh size in the propagation direction is 0.09 mm . The mesh is coarser than the one used for the DCB because the process zone in mixed mode is larger than in mode I. The width of the model is $1/10$ of the width of the specimen, so the force results presented in the results were scaled up to the full width. The loading lever was modeled using a multi-point constraint equation that enforces the relative vertical motion of the three points of contact. A length of the loading arm $c = 41.28 \text{ mm}$ corresponds to a mode mixity of 50% [40].

Table 5. Dimensions of MMB specimen in mm.

a_0	b	h	L	c
28.83	25.4	2.27	101.6	41.28

The material properties applied to the model are those previously reported in Table 4. No bridging was applied because the R-curve for mode II was not available. The analyses were conducted under force control, as was done during the characterization test [39].

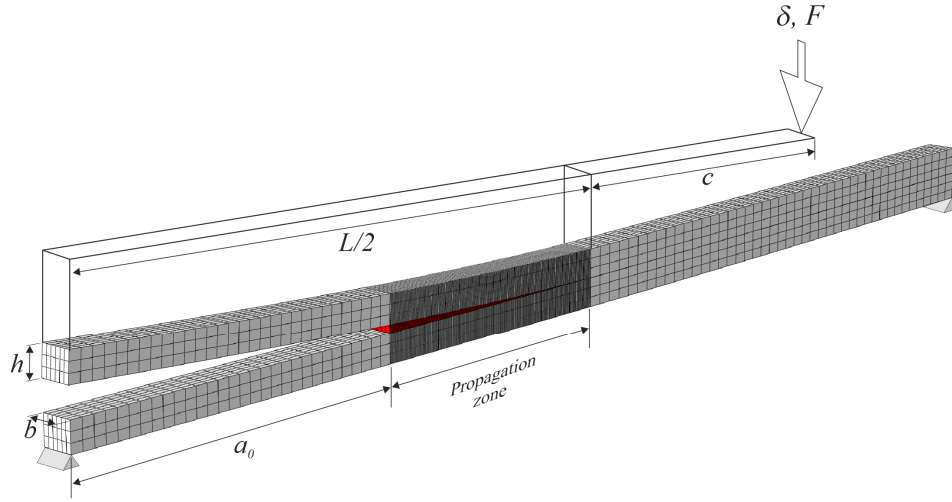


Fig. 23. Finite element model of MMB specimen.

A closed form expression such as Eq. 26 for the crack length as a function of compliance is not available for the MMB specimen. Therefore, a quadratic polynomial was generated to fit the results of analyses with different crack lengths. For a 25.4 mm-wide specimen, the crack length is:

$$a = -3.37 \cdot 10^5 \left(\frac{\delta}{F} \right)^2 + 8.55 \cdot 10^3 \frac{\delta}{F} - 1.572 \quad (30)$$

The results of three analyses are shown in Fig. 24 along with test data. The analysis results are shown as solid lines and the test data are represented by the marker symbols. The analyses correspond to applied forces of $F = 170, 193, \text{ and } 222$ N. At the beginning of the analysis, these forces correspond to G/G_c of 0.26, 0.32, and 0.43, respectively. As the crack lengths increase, so do the relative ERR. As in the case of the DCB specimen, the propagation rates are initially high, and decrease once the process zone is formed. The process zone length during steady-state propagation, which is the band of partially damaged cohesive elements, is 1.1 mm. The symbols on the curves represent the onset point for a 5% increase in compliance. The three points in the simulations line up along a Paris law.

The propagation rate decreases near the end of each simulation, which occurs when the crack approaches the center of the specimen, where the support of the lever arm presses down on the upper arm and the loading condition changes. One of the experimental curves shown in Fig. 24 exhibits this reduction in the propagation rates.

The location of the initial and steady-state values of the critical ERR are also shown for reference. According to the measurements of Ratcliffe [39], the R-curve for a 50% mode mixity starts at 0.355 N-mm/mm², and reaches 0.435 N-mm/mm² after 4 mm of propagation. Since the model is based on the properties of mode I and mode II fracture, these values of the G_R at 50% mode mixity were not used in the analysis. As stated earlier, a bridging law was not used in the analyses because the R-curve in mode II was not available. It is expected that adding a bridging law would decrease somewhat the propagation rates during the latter parts of the simulations, which would improve the correlation between predicted and test data.

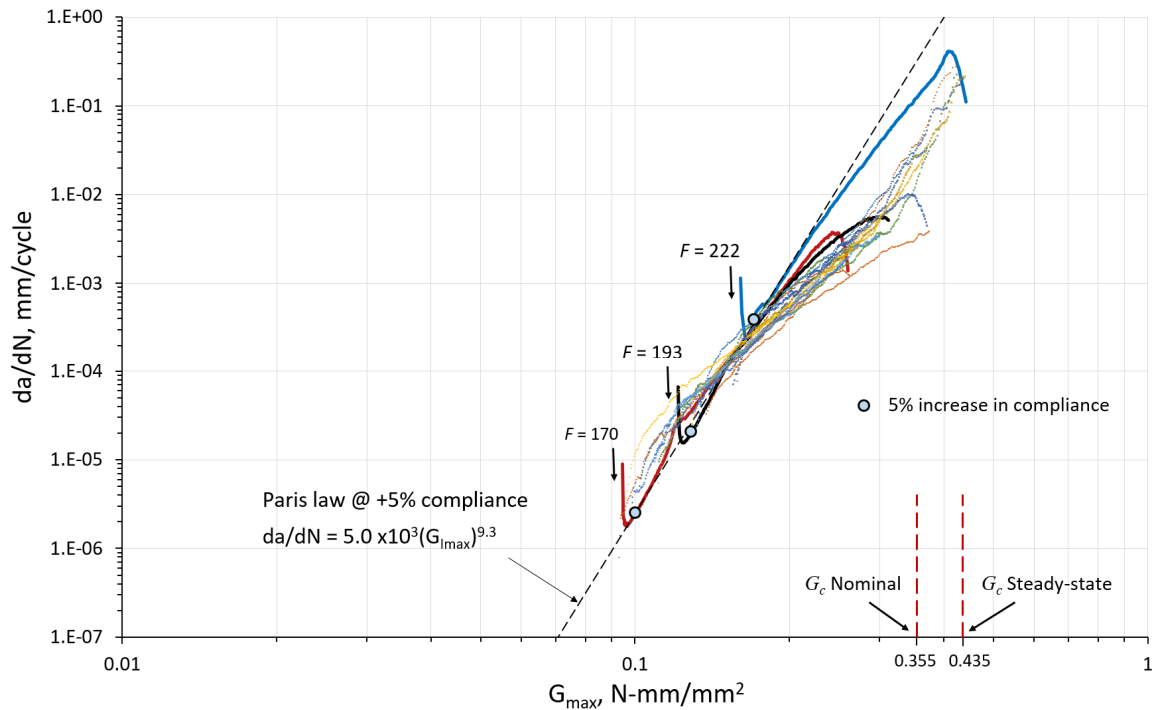


Fig. 24. Delamination growth rates in 50% mixed mode for three applied forces and $R = 0.1$.

3.3 Relationships between Material Properties

The results of the analyses presented herein highlight a number of relationships between the various properties that characterize the response of a material under quasi-static and fatigue loading. Relationships have emerged between the stress ratio R and the following: the endurance limit (Eq. 6), the exponent β of the damage model (Eq. 12), and the slope of the Paris law (Eq. 29). A plot of the exponent m of the Paris law as a function of β for the results in Figs. 21 and 24 is shown in Fig. 25, where a linear relation between these two values can be observed. A linear relationship between these two coefficients had been predicted by Vieira [24] using theoretical considerations. Using a mode II damage evolution model, Allegri [41] calculated $m = \beta/2$, which is a good approximation for the mode I and mixed mode results obtained by the present analyses.

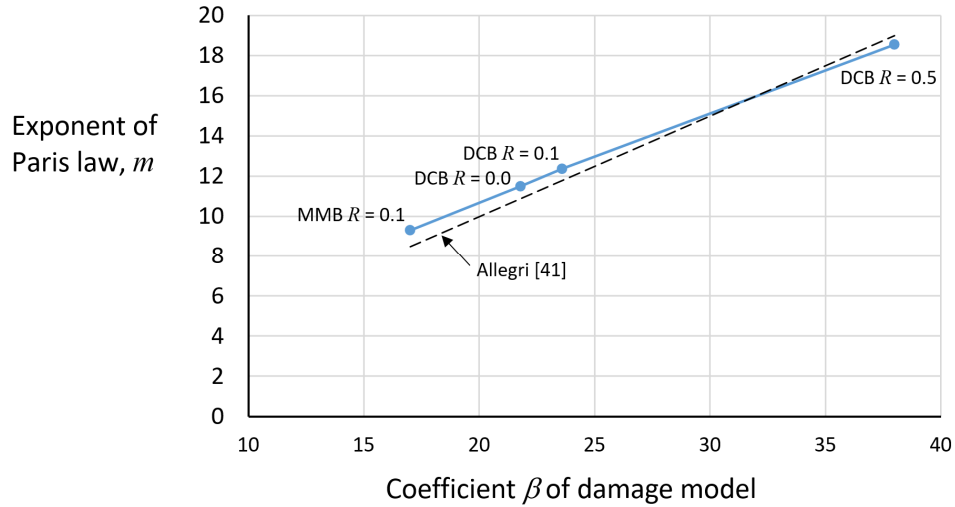


Fig. 25. Predicted exponent m of the Paris law vs. exponent of the damage model.

The simple relationships between β and m suggest that the slope of the Paris law is a function of the S-N diagram and all of the considerations discussed in Section 2 that were used to establish it, including the effects of the stress ratio and the mode mixity. A study of the relationship between m and the mode mixity may help establish accurate interpolation procedures for the coefficients of the Paris law for intermediate values of the mode mixity [42].

The results of parametric studies indicate that the coefficient C of the Paris law is a function of factors that do not affect m , including the strength σ_c and the critical energy release, G_c . To illustrate the sensitivity of the predicted propagation rate on these two material properties, two analyses of the DCB specimen were performed in which σ_c and G_c were increased by 50% over their nominal values. In the first analysis, the strength was increased from 80 MPa to 120 MPa, while all other properties remained at their nominal values. In the second analysis, G_c was increased from 0.24 N-mm/mm² to 0.36 N-mm/mm². No bridging was applied in these analyses. The mesh for the analysis where the strength was increased was doubled in all directions compared to the model described in Section 3.1.1 to account for the expected decrease of the process zone size that accompanies an increase in strength. The results of the analyses are compared to the nominal results in Fig. 26. Paris lines were fit through the predicted propagation rates, and the coefficients C of the lines are used to calculate the relative propagation rates. The predicted crack propagation rate for a 50% increase in strength is 2.6 times slower than predicted with the nominal strength value, and the predicted rate for a 50% increase in G_c is 94 times slower than predicted with the nominal G_c value.

Other factors were also found to affect the value of C . For instance, the results of exploratory analyses (not shown) suggest that reducing the thickness of the arms of the DCB from 2.25 mm to 1 mm causes a 25% reduction in the rate of crack propagation. Finally, the form of the damage accumulation model also affects the coefficient C of the propagation rate. The particular form of the damage accumulation model in Eq. 8 was selected for its ability to reproduce the S-N diagram and the Paris law. However, additional studies are needed to develop a fatigue damage accumulation model based on a physical understanding of the fatigue damage processes.

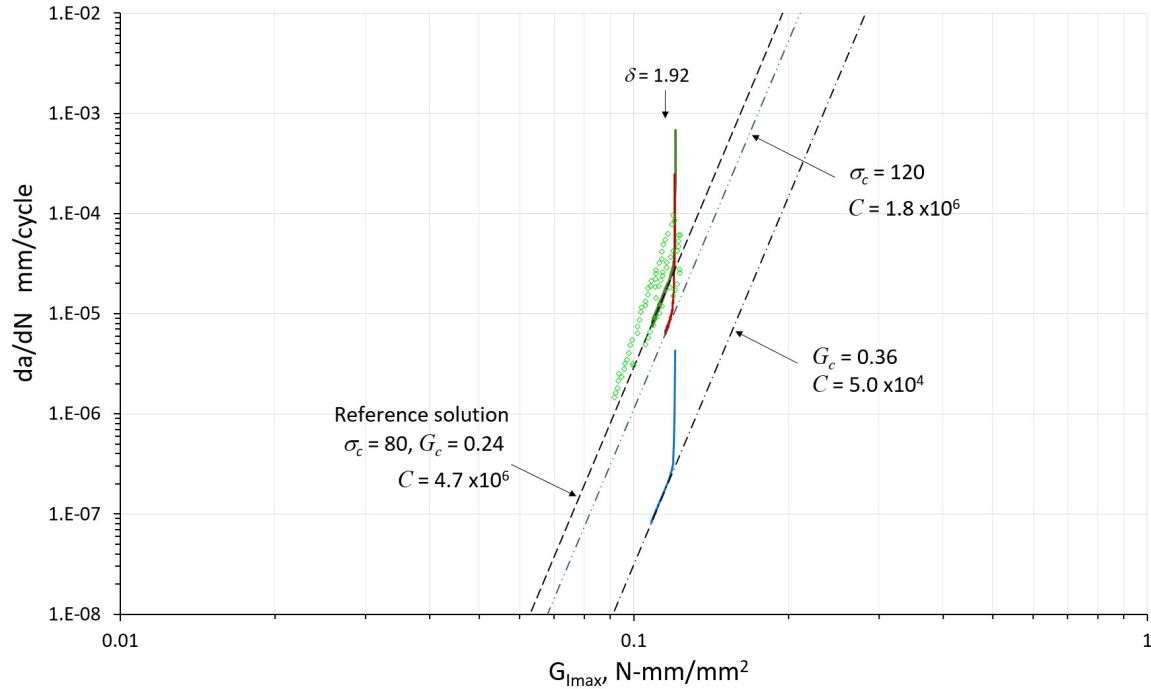


Fig. 26. Predicted fatigue delamination propagation rates for DCB specimen with nominal properties compared to predicted fatigue crack propagation rates with either strength or critical ERR increased by 50%.

4 Summary and Discussion

The relationships between the material properties that describe tearing (G_c , σ_c), those that describe fatigue life (S-N), those that describe crack onset (G-N), and those that describe crack propagation rates (Paris law) are explored using a new cohesive fatigue damage model. The model relies on the former two characterizations (tearing and life) to predict the latter two (onset and Paris law). The proposed fatigue model assumes that a single variable is sufficient to represent the historical effects of load cycles on damage at a material point, regardless of whether the damage was caused by tearing or by fatigue. With this assumption, the quasi-static cohesive law becomes the envelope of the fatigue law. Fatigue damage inside the envelope accumulates at a rate that depends on the displacement jumps. The damage model relies on the simplicity of typical S-N diagrams and the fact that the endurance limit can often be estimated from the quasi-static strength without performing any fatigue tests. The two parameters required by the model, β and γ , are extracted from the quasi-static properties and the S-N idealizations.

The heuristic constitutive fatigue damage model was implemented as a user-written subroutine UMAT for Abaqus using Turon's mixed-mode cohesive law. The particular form of the constraints imposed between mode I and mode II in the Turon cohesive model, which are necessary to ensure thermodynamic consistency in mixed mode, allow an effortless implementation of the fatigue damage model in mixed mode.

The predictive capability of the fatigue model was evaluated by comparing predicted crack propagation rates in DCB and MMB specimens composed of IM7/8552 graphite/epoxy material

with experimental data. A technique based on the superposition of two cohesive laws was applied to represent the R-curve effect observed in the DCB experiments. The results of the model capture the lateral shifting of the propagation curves that was observed experimentally.

The fatigue cohesive model that is proposed is capable of predicting interfacial failure in unnotched problems where life and S-N diagrams dominates the physics of the problem, and it can also predict crack propagation rates, where the Paris law is typically used. The model seamlessly bridges the gap between tearing, life, crack onset, and fatigue propagation. The fact that all of the fatigue predictions were conducted without experimental fatigue data is unique about the proposed model and methodology. The fatigue response is a result of material-independent idealizations of S-N diagrams as well as the quasi-static strength and fracture properties. Although the predictions of the propagation rates predicted for IM7/8552 are in good agreement with the experimental results, additional work is necessary to validate the present model for different materials and loading conditions.

References

1. Juvinall, R. C., and Marshek, K. M., *Fundamentals of Machine Component Design*, Wiley, New York, NY, 2000.
2. Shigley, J. E., and Mitchell, L. D., *Mechanical Engineering Design*, McGraw-Hill Book Company, New York, NY, 1983.
3. Krueger, R., "Virtual Crack Closure Technique: History, Approach, and Applications," *Applied Mechanics Reviews*, Vol. 57, No. 2, 2004, pp. 109-143.
4. Dassault Systèmes, *Abaqus® 2017 Documentation*, Simulia Corp., Providence, RI, USA, 2017.
5. Bisagni, C., Brambilla, P., and Dávila, C. G., "Modeling Delamination in Postbuckled Composite Structures under Static and Fatigue Loads," SAMPE Conference, Long Beach, CA, USA, 6-9 May 2013.
6. De Carvalho, N. V., Krueger, R., Mabson, G. E., and Deobald, L., "Combining Progressive Nodal Release with the Virtual Crack Closure Technique to Model Fatigue Delamination Growth without Re-Meshing," Proceedings of the 2018 AIAA/ASCE/AHS/ASC Structures, Structural Dynamics, and Materials Conference, Kissimmee, FL, 8–12 January 2018, pp. 1468.
7. Bažant, Z. P., and Chen, E.-P., "Scaling of Structural Failure," Sandia National Laboratories, Sandia Report SAND96-2948, Albuquerque, NM, Dec. 1996.
8. Bak, B. L. V., Turon, A., Lindgaard, E., and Lund, E., "A Benchmark Study of Simulation Methods for High-Cycle Fatigue-Driven Delamination Based on Cohesive Zone Models," *Composite Structures*, Vol. 164, 2017, pp. 198-206.
9. Turon, A., Costa, J., Camanho, P. P., and Dávila, C. G., "Simulation of Delamination in Composites under High-Cycle Fatigue," *Composites Part A: Applied Science and Manufacturing*, Vol. 38, No. 11, 2007, pp. 2270-2282.
10. Bak, B. L. V., Turon, A., Lindgaard, E., and Lund, E., "A Simulation Method for High-Cycle Fatigue-Driven Delamination Using a Cohesive Zone Model," *International Journal for Numerical Methods in Engineering*, Vol. 106, No. 3, 2016, pp. 163-191.

11. Iarve, E. V., Hoos, K., Braginsky, M., Zhou, E., and Mollenhauer, D. H., "Progressive Failure Simulation in Laminated Composites under Fatigue Loading by Using Discrete Damage Modeling," *Journal of Composite Materials*, Vol. 51, No. 15, 2017, pp. 2143-2161.
12. Voormeeren, L. O., van der Meer, F. P., Maljaars, J., and Sluys, L. J., "A New Method for Fatigue Life Prediction Based on the Thick Level Set Approach," *Engineering Fracture Mechanics*, Vol. 182, 2017, pp. 449-466.
13. Peerlings, R. H. J., Brekelmans, W. A. M., de Borst, R., and Geers, M. G. D., "Gradient-Enhanced Damage Modelling of High-Cycle Fatigue," *International Journal for Numerical Methods in Engineering*, Vol. 49, No. 12, 2000, pp. 1547-1569.
14. Nguyen, O., Repetto, E. A., Ortiz, M., and Radovitzky, R. A., "A Cohesive Model of Fatigue Crack Growth," *International Journal of Fracture*, Vol. 110, No. 4, 2001, pp. 351-369.
15. Maiti, S., and Geubelle, P. H., "A Cohesive Model for Fatigue Failure of Polymers," *Engineering Fracture Mechanics*, Vol. 72, No. 5, 2005, pp. 691-708.
16. Nojavan, S., Schesser, D., and Yang, Q. D., "An in Situ Fatigue-Czm for Unified Crack Initiation and Propagation in Composites under Cyclic Loading," *Composite Structures*, Vol. 146, No. Supplement C, 2016, pp. 34-49.
17. Bak, B. L., Sarrado, C., Turon, A., and Costa, J., "Delamination under Fatigue Loads in Composite Laminates: A Review on the Observed Phenomenology and Computational Methods," *Applied Mechanics Reviews*, Vol. 66, No. 6, 2014, p. 060803.
18. Lemaitre, J., *A Course on Damage Mechanics*, Springer-Verlag, Second Edition, Berlin, Germany, 1996.
19. Dávila, C. G., Camanho, P. P., and de Moura, M. F. S. F., "Mixed-Mode Decohesion Elements for Analyses of Progressive Delamination," Paper AIAA-01-1486, 42nd AIAA/ASME/ASCE/AHS/ASC Structures, Structural Dynamics and Materials Conference, Seattle, WA, 16-19 April 2001.
20. O'Brien, T. K., Chawan, A. D., Krueger, R., and Paris, I. L., "Transverse Tension Fatigue Life Characterization through Flexure Testing of Composite Materials," *International Journal of Fatigue*, Vol. 24, No. 2-4, 2002, pp. 127-145.
21. Fleck, N. A., Kang, K. J., and Ashby, M. F., "Overview No. 112: The Cyclic Properties of Engineering Materials," *Acta Metallurgica et Materialia*, Vol. 42, No. 2, 1994, pp. 365-381.
22. Goodman, J., *Mechanics Applied to Engineering*, Longmans, Green and Co., London, UK, 1899.
23. *CES Selector Software*, Granta Design Limited, Cambridge, UK, 2017.
24. Vieira, A. P., Andrade, J. S., and Herrmann, H. J., "Subcritical Crack Growth: The Microscopic Origin of Paris' Law," *Physical Review Letters*, Vol. 100, No. 19, 2008, p. 195503.
25. Kun, F., Carmona, H. A., Andrade, J. S., and Herrmann, H. J., "Universality Behind Basquin's Law of Fatigue," *Physical Review Letters*, Vol. 100, No. 9, 2008, p. 094301.
26. Turon, A., González, E. V., Sarrado, C., Guillaumet, G., and Maimí, P., "Accurate Simulation of Delamination under Mixed-Mode Loading Using a Cohesive Model with a Mode-Dependent Penalty Stiffness," *Composite Structures*, Vol. 184, No. Supplement C, 2018, pp. 506-511.
27. ASTM D5528-01, "Standard Test Method for Mode I Interlaminar Fracture Toughness of Unidirectional Fiber-Reinforced Polymer Matrix Composites," *Annual Book of ASTM Standards*, American Society for Testing and Materials, West Conshohocken, PA, 2002.
28. Murri, G. B., "Evaluation of Delamination Onset and Growth Characterization Methods under Mode I Fatigue Loading," Technical Report NASA/TM-2013-217966, Hampton, VA, Feb. 2013.

29. Brunner, A. J., Murphy, N., and Pinter, G., "Development of a Standardized Procedure for the Characterization of Interlaminar Delamination Propagation in Advanced Composites under Fatigue Mode I Loading Conditions," *Engineering Fracture Mechanics*, Vol. 76, No. 18, 2009, pp. 2678-2689.
30. Wanthal, S., Schaefer, J., Justusson, B., Hyder, I., Engelstad, S., and Rose, C. A., "Verification and Validation Process for Progressive Damage and Failure Analysis Methods in the NASA Advanced Composites Consortium," American Society for Composites Technical Conference, Purdue University, West Lafayette, IN, 23-25 Oct. 2017.
31. Reeder, J. R., Demarco, K., and Whitley, K. S., "The Use of Doubler Reinforcement in Delamination Toughness Testing," *Composites Part A: Applied Science and Manufacturing*, Vol. 35, No. 11, 2004, pp. 1337-1344.
32. ASTM D 6115 – 97, "Standard Test Method for Mode I Fatigue Delamination Growth Onset of Unidirectional Fiber-Reinforced Polymer Matrix Composites," *Annual Book of ASTM Standards*, American Society for Testing and Materials, West Conshohocken, PA, 2002.
33. Yao, L., Alderliesten, R., Zhao, M., and Benedictus, R., "Bridging Effect on Mode I Fatigue Delamination Behavior in Composite Laminates," *Composites Part A: Applied Science and Manufacturing*, Vol. 63, 2014, pp. 103-109.
34. Dávila, C. G., Rose, C. A., and Camanho, P. P., "A Procedure for Superposing Linear Cohesive Laws to Represent Multiple Damage Mechanisms in the Fracture of Composites," *International Journal of Fracture*, Vol. 158, No. 2, 2009, pp. 211-223.
35. Airoidi, A., and Dávila, C. G., "Identification of Material Parameters for Modelling Delamination in the Presence of Fibre Bridging," *Composite Structures*, Vol. 94, No. 11, 2012, pp. 3240-3249.
36. Martin, R. E., and Murri, G. B., "Characterization of Mode I and Mode II Delamination Growth and Thresholds in Graphite/Peek Composites," NASA-TM-100577, Hampton, VA, April 1988.
37. Andersons, J., Hojo, M., and Ochiai, S., "Empirical Model for Stress Ratio Effect on Fatigue Delamination Growth Rate in Composite Laminates," *International Journal of Fatigue*, Vol. 26, No. 6, 2004, pp. 597-604.
38. Allegri, G., Wisnom, M. R., and Hallett, S. R., "A New Semi-Empirical Law for Variable Stress-Ratio and Mixed-Mode Fatigue Delamination Growth," *Composites Part A: Applied Science and Manufacturing*, Vol. 48, 2013, pp. 192-200.
39. Ratcliffe, J. G., and Johnston Jr, W. M., "Influence of Mixed Mode I-Mode II Loading on Fatigue Delamination Growth Characteristics of a Graphite Epoxy Tape Laminate," Proceedings of the 29th American Society for Composites Technical Conference, La Jolla, CA, 8-10 Sep 2014.
40. ASTM_D6671/D6671M, "Standard Test Method for Mixed Mode I-Mode II Interlaminar Fracture Toughness of Unidirectional Fiber Reinforced Polymer Matrix Composites," *Annual Book of ASTM Standards*, American Society for Testing and Materials, West Conshohocken, PA, 2006.
41. Allegri, G., and Wisnom, M. R., "A Non-Linear Damage Evolution Model for Mode II Fatigue Delamination Onset and Growth," *International Journal of Fatigue*, Vol. 43, 2012, pp. 226-234.
42. Lyle, D. R., Mabson, G. E., Engelstad, S., Rao, M. P., Gurvich, M., Seneviratne, W., Perera, S., O'Brien, T. K., Murri, G., Ratcliffe, J. G., Dávila, C. G., Carvalho, N., and Krueger, R., "Guidelines for VCCT-Based Interlaminar Fatigue and Progressive Failure Finite Element Analysis," NASA/TM–2017-219663, Hampton, VA, Sept. 2017.

Appendix A: Numerical Determination of Fatigue Damage Coefficients β and γ

The coefficients β and γ of the fatigue damage model are obtained by solving the nonlinear system of two equations obtained by enforcing the number of cycles to failure, N^f , at two anchor points along an S-N curve. The first point defines the low-cycle end of the S-N curve, and the second point is the endurance limit. In the present work, these points are defined as:

$$@ \sigma^{\max} / \sigma_c = 0.99 \quad N^f = 2 \text{ cycles} \quad (\text{B1})$$

$$@ \sigma^{\max} / \sigma_c = 1/(2-R) \quad N^f = 1.10^7 \text{ cycles} \quad (\text{B2})$$

where the number of cycles at failure N^f is calculated as

$$N^f = \left(\frac{\sigma_c}{\sigma^{\max}} \right)^\beta \int_0^{D^F} \frac{(1-D)^{-\beta}}{D+\gamma} dD, \quad \text{where} \quad D^F = 1 - \frac{\sigma^{\max}}{\sigma_c} \quad (\text{B3})$$

The methodology presented in this report is not valid for negative R ratios in mode I or in mixed mode because contact conditions prevent a reversal of the opening displacements. However, the effective R^{eff} ratio, which takes into account for the effect of mode mixity B can be negative. The R^{eff} ratio is defined as:

$$R^{eff} = \frac{R-2}{1-0.42B} + 2 \quad (\text{B4})$$

Therefore, for a range of stress ratio $0 < R < 1$, the range of R^{eff} is $-1.45 < R^{eff} < 1$. The values of β and γ shown in Fig. A1 were calculated with a simple program that searches for the values that minimize the error in N^f .

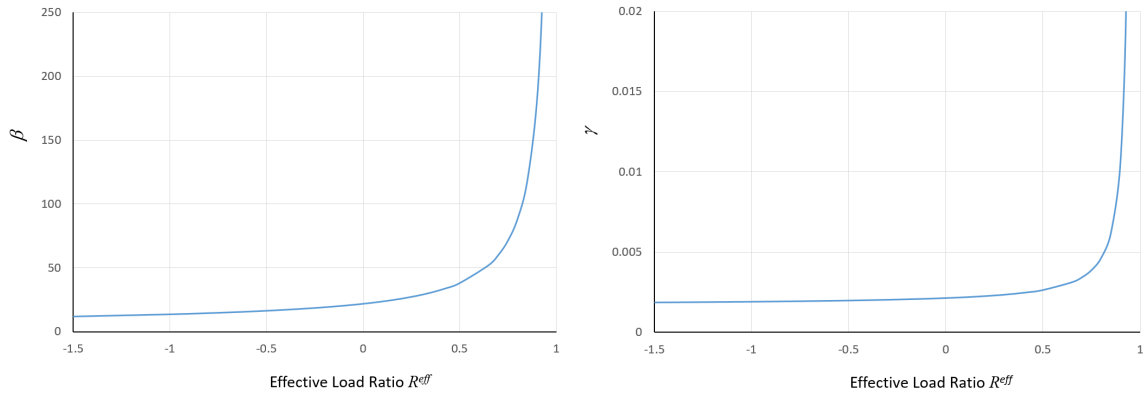


Fig. A1. Calculated values of the coefficients β and γ of the fatigue damage model.

REPORT DOCUMENTATION PAGE

Form Approved
OMB No. 0704-0188

The public reporting burden for this collection of information is estimated to average 1 hour per response, including the time for reviewing instructions, searching existing data sources, gathering and maintaining the data needed, and completing and reviewing the collection of information. Send comments regarding this burden estimate or any other aspect of this collection of information, including suggestions for reducing the burden, to Department of Defense, Washington Headquarters Services, Directorate for Information Operations and Reports (0704-0188), 1215 Jefferson Davis Highway, Suite 1204, Arlington, VA 22202-4302. Respondents should be aware that notwithstanding any other provision of law, no person shall be subject to any penalty for failing to comply with a collection of information if it does not display a currently valid OMB control number.
PLEASE DO NOT RETURN YOUR FORM TO THE ABOVE ADDRESS.

1. REPORT DATE (DD-MM-YYYY) 1-06-2018		2. REPORT TYPE Technical Publication		3. DATES COVERED (From - To)	
4. TITLE AND SUBTITLE From S-N to the Paris Law with a New Mixed-Mode Cohesive Fatigue Model				5a. CONTRACT NUMBER	
				5b. GRANT NUMBER	
				5c. PROGRAM ELEMENT NUMBER	
6. AUTHOR(S) Davila, Carlos G.				5d. PROJECT NUMBER	
				5e. TASK NUMBER	
				5f. WORK UNIT NUMBER 826611.04.07.01	
7. PERFORMING ORGANIZATION NAME(S) AND ADDRESS(ES) NASA Langley Research Center Hampton, VA 23681-2199				8. PERFORMING ORGANIZATION REPORT NUMBER L-20933	
9. SPONSORING/MONITORING AGENCY NAME(S) AND ADDRESS(ES) National Aeronautics and Space Administration Washington, DC 20546-0001				10. SPONSOR/MONITOR'S ACRONYM(S) NASA	
				11. SPONSOR/MONITOR'S REPORT NUMBER(S) NASA-TP-2018-219838	
12. DISTRIBUTION/AVAILABILITY STATEMENT Unclassified Subject Category 24 Availability: NASA STI Program (757) 864-9658					
13. SUPPLEMENTARY NOTES					
14. ABSTRACT The relationship between fatigue life and fatigue crack propagation rate is explored with a new cohesive damage model. The parameters of the model are obtained from idealizations of S-N diagrams used in engineering design. The model is based on the hypothesis that both stable tearing damage and damage due to cyclic loading are representations of a density of microcracks and, therefore, a single damage variable can describe the state of damage. This assumption implies that the quasi-static cohesive law that describes tearing is also the envelope of the fatigue damage. Fatigue damage within the cohesive envelope is assumed to accumulate at a rate that depends on the displacement jumps. The fatigue model was implemented as a UMAT subroutine for Abaqus cohesive elements by adding fatigue damage accumulation to a cohesive model based on the Turon mixed-mode cohesive laws. The analyses were conducted using a simplified cyclic loading procedure in which the maximum applied load is kept constant and the computational expense of cycling the load is avoided. The predicted propagation rates in mode I and mixed mode were compared to experimental results for IM7/8552 graphite/epoxy tape. Several aspects of the results were investigated, including the effect of R-curves, the stress ratio R, and the difference between displacement control and force control.					
15. SUBJECT TERMS Mixed-mode cohesive fatigue model; Paris law					
16. SECURITY CLASSIFICATION OF:			17. LIMITATION OF ABSTRACT	18. NUMBER OF PAGES	19a. NAME OF RESPONSIBLE PERSON
a. REPORT	b. ABSTRACT	c. THIS PAGE			STI Help Desk (email: help@sti.nasa.gov)
U	U	U	UU	40	19b. TELEPHONE NUMBER (Include area code) (757) 864-9658